Biomechanics and Modeling in Mechanobiology (2018) 17:1243–1268
https://doi.org/10.1007/s10237-018-1023-x

ORIGINAL PAPER

Three-dimensional simulation of obstacle-mediated chemotaxis

Adrian Moure[1] · **Hector Gomez**[1]

Received: 16 September 2017 / Accepted: 25 April 2018 / Published online: 4 May 2018

Abstract
Amoeboid cells exhibit a highly dynamic motion that can be directed by external chemical signals, through the process of chemotaxis. Here, we propose a three-dimensional model for chemotactic motion of amoeboid cells. We account for the interactions between the extracellular substances, the membrane-bound proteins, and the cytosolic components involved in the signaling pathway that originates cell motility. We show two- and three-dimensional simulations of cell migration on planar substrates, flat surfaces with obstacles, and fibrous networks. The results show that our model reproduces the main features of chemotactic amoeboid motion. Our simulations unveil a complicated interplay between the geometry of the cell's environment and the chemoattractant dynamics that tightly regulates cell motion. The model opens new opportunities to simulate the interactions between extra- and intra-cellular compounds mediated by the matrix geometry.

Keywords Amoeboid motion · Chemotaxis · Phase-field modeling · 3D cell migration

1 Introduction

Cells in the human body may display a motile behavior that is essential for life. Processes such as tissue growth, cancer metastasis, or wound healing cannot be accomplished without cell motion. An outstanding feature of motile cells is their ability to perceive external stimuli that can direct their motion. Durotaxis (Sunyer et al. 2016), haptotaxis, or electrotaxis are prime examples of directed cellular motion. In this paper, we study chemotaxis, which is the movement of cells guided by chemical cues. We focus on *Dictyostelium discoideum*, which migrates spontaneously but also undergoes chemotaxis when subject to extracellular chemotactic factors (e.g., a gradient of cAMP; see Song et al. 2006). *Dictyostelium* performs amoeboid motion (Lämmermann and Sixt 2009), which follows the five-step model of cell migration (Friedl and Wolf 2003). Amoeboid cell motility may be identified by its extraordinary deformability and dynamism, which results from a balance between myosin-induced contraction and rapid membrane extensions. These highly localized membrane protrusions are caused by the emergence of dense actin networks, called pseudopods. Pseudopod extension is driven by actin polymerization, which is regulated by several intracellular pathways (Dawes and Edelstein-Keshet 2007) affected by extracellular signals. The prevalent model of chemotaxis assumes that pseudopod formation is caused by chemotactic signals. That approach does not explain behaviors such as, e.g., spontaneous migration. Therefore, we follow the pseudopod-centered view (Insall 2010) that considers pseudopod formation as a self-generated process that does not require external signals. When external chemical signals are indeed present they bias the location of growing and retracting pseudopods.

Chemotaxis arises with the association between the extracellular factors and the membrane receptors. Variations in the number of bound receptors produce the reactions between the signaling pathways that generate a chemotactic response (Van Haastert and Devreotes 2004; Swaney et al. 2010). Computational modeling of cell signaling usually focuses on a single pathway. Starting with the extracellular signal, the models provide the chemotactic response to the cytosolic machinery. This kind of models accounts for the reactions occurring in the vicinity of the membrane and may exhibit different levels of complexity. For example, the model presented in Meinhardt (1999) includes a global and a local inhibitors, and an activator that provides the response. Levchenko and Iglesias (2002) proposed a more complex

Electronic supplementary material The online version of this article (https://doi.org/10.1007/s10237-018-1023-x) contains supplementary material, which is available to authorized users.

✉ Adrian Moure
amourero@purdue.edu

[1] School of Mechanical Engineering, Purdue University, 585 Purdue Mall, West Lafayette, IN 47907, USA

model that accounts for adaptation and signal amplification; see also Subramanian and Narang (2004) and Gamba et al. (2005). All of these models consider a fixed geometry for the cell and restrict the signaling reactions to the membrane compounds.

Taking into account cell deformation requires the use of novel methods that entail computational challenges. The cellular potts model (Marée et al. 2012) or the use of moving bulk and surface meshes (MacDonald et al. 2016) are examples where the dynamics of the signaling molecules are posed on moving cells. In particular, Elliott et al. (2012) solves the equations proposed by Meinhardt (1999) on an evolving surface that moves according to the activator response. The immersed boundary method (Liu et al. 2006; Strychalski et al. 2015; Casquero et al. 2017) that resorts to a moving Lagrangian mesh and a fixed Eulerian mesh also permits to account for time-evolving cell geometries. To avoid the algorithmic complexity of the use of moving meshes, the level set (Neilson et al. 2011; Shi et al. 2013) and the phase-field (Moure and Gomez 2017) methods offer an alternative: they employ a single fixed mesh where an auxiliary field identifies the region occupied by the cell. In this paper, we use the phase-field (or diffuse domain) method that, besides tracking the cell, permits the localization of the evolution laws of different compounds to the region where they take place; namely the cytosol, the membrane, or the extracellular medium.

The chemotactic pathway does not end with the response given by the membrane-signaling molecules. Chemotaxis finalizes with the motion of the cell, which is accomplished by the cytosolic machinery, mainly by remodeling the actomyosin network. Thus, the bidirectional feedback between the cytosolic elements and the membrane proteins plays a crucial role (Van Haastert and Devreotes 2004). However, while there is a significant body of literature that studies models of the membrane signaling compounds such as, e.g., Hecht et al. (2011), Shi et al. (2013) and Vermolen and Gefen (2013), their interaction with the cellular motile machinery has been overlooked. The coupling between the membrane and the cytosolic compounds has been recently included in works such as Marth and Voigt (2014) or Moure and Gomez (2016) which focus on non-chemotactic migration. Models of chemotactic migration have traditionally focused on two-dimensional approaches. It has been recognized that quantitative agreement with experiments will require a refinement of the biochemical mechanisms accounted for in the model, but also three-dimensional simulations. Significant progress has been made in this direction in recent years (Allena and Aubry 2012; Elliott et al. 2012; Vermolen and Gefen 2013; Tjhung et al. 2015), but the current state of the art does not yet permit to model cell migration in a collagen matrix (Chen et al. 2014).

This paper proposes a model of individual amoeboid motion driven by chemotactic signals. The model considers cell migration in three-dimensional environments with rigid obstacles and fibers. Our results reveal a complicated interplay between the matrix geometry and the chemoattractant dynamics that strongly regulate the cell's motion. From a methodological point of view we build on our earlier modeling work (Moure and Gomez 2016, 2017). The objective of our previous publications was to understand the importance of the cytosol-membrane coupling and spontaneous 3D migration on fibrous environments. Here, our goal is to understand the complicated interactions between the chemoattractant and the matrix geometry in obstacle-mediated chemotaxis. We take into account the biomechanics of the main cytosolic components involved in cell motility. We also track the dynamics of the membrane-signaling molecules and locate the chemotactic factors to the extracellular environment. Since we employ the diffuse domain method, we only need a fixed mesh to solve the continuous problem. In addition, the force balance equation posed on the actomyosin network permits the incorporation of the forces arising from the cell-substrate and cell-fiber interactions. The reactions of the signaling cascade are simplified by resorting to a stochastic process that accounts for pseudopod formation.

This paper is organized as follows: we first present the model for chemotactic migration of *Dictyostelium*. Then, we briefly explain the numerical method employed to solve the problem. We analyze the influence of the chemoattractant distribution on the motion of the cells. We also show results where natural cAMP waves guide cell migration. In addition, we present a 3D simulation of a cell migrating in a fibrous network. Finally, we review the main limitations of the model and draw some conclusions.

2 Model of chemotactic amoeboid motion

We propose a mathematical model for chemotactic amoeboid motion based on our previous works for spontaneous migration; see Moure and Gomez (2016, 2017). The model resorts to the diffuse domain method to track the cell, the membrane, and the extracellular medium; as well as to locate the dynamics of the components living on each domain. We organize the model into four blocks: cell motion; biomechanics of the cytosolic compounds; dynamics of the extracellular ligand; and dynamics of a generic membrane-bound activator.

2.1 Diffuse domain approach

In our problem, the moving cell determines two different regions that change in time: the cell itself and the extracellular environment. Here, we consider a fixed domain Ω that encloses both time-dependent regions. We make use of the diffuse domain method (Li et al. 2009; Gomez and

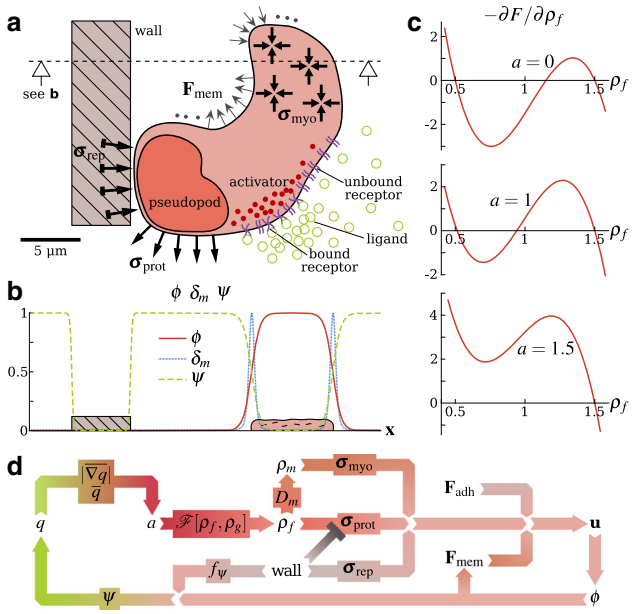

Fig. 1 Cell motion and diffuse domain method. **a** Cell forces and membrane-signaling reactions. **b** Diffuse domain approach. Description of the cell, the cellular membrane, and the extracellular environment. **c** Dependence of the actin free-energy functional on the activator. **d** Main interactions between the model compounds and terms driving those interactions

van der Zee 2017) to distinguish each region. In particular, we employ the phase-field variable $\phi(\mathbf{x}, t)$ for cell location, and then we define membrane and extracellular markers by means of ϕ.

2.1.1 Cell motion

The phase-field variable ϕ defines the location of the cell such that $\phi \approx 1$ inside the cell and $\phi \approx 0$ outside the cell (see Fig. 1a, b). The interface (i.e, the cell membrane) displays a smooth transition from 0 to 1 over a width defined by a length scale ε. The movement of the membrane is driven by the velocity of the F-actin network $\mathbf{u}$. The evolution equation for ϕ is

$$\frac{\partial \phi}{\partial t} + \mathbf{u} \cdot \nabla \phi = \Gamma_\phi \left(\varepsilon \nabla^2 \phi - \frac{G'(\phi)}{\varepsilon} + c\varepsilon |\nabla \phi| \right), \tag{1}$$

where $G(\phi) = 18\phi^2(1-\phi)^2$ is a double-well potential with minima at 0 and 1, Γ_ϕ is a constant, and $c = \nabla \cdot \mathbf{n}$ is the mean curvature of the membrane with $\mathbf{n} = -\nabla\phi/|\nabla\phi|$ the unit normal vector. Equation (1) is a modified Allen–Cahn equation (see Biben et al. 2005) that may be thought of as a perturbed level set equation. The perturbation is given by the right-hand side of Eq. (1), which is $\mathscr{O}(\varepsilon)$. The equation leads to motion of the level set $\phi = 1/2$ with velocity $\mathbf{u}$, while the interface between 0 and 1 maintains a hyperbolic tangent profile. Equation (1) is a non-conservative equation that allows changes in cell volume.

2.1.2 Membrane marker

The membrane of the cell can be located by employing a smooth function δ_m that takes the value ~ 1 on the membrane and ~ 0 elsewhere. By making use of the phase-field variable ϕ, we define the marker

$$\delta_m(\phi) = \exp[-\varphi(\phi - 1/2)^2], \tag{2}$$

which has been plotted in Fig. 1b. The thickness of the marker is controlled by the parameter φ.

2.1.3 Extracellular marker

Our model considers the presence of obstacles to the cell's motion that represent a simplified notion of the extracellular matrix or external barriers to motility. We consider that these obstacles do not permit the diffusion of any extracellular substance through them. Therefore, we locate regions outside the cell and the obstacles with the spatial marker

$$\psi(\phi, d_o(\mathbf{x})) = (1-\phi) f_\psi(d_o(\mathbf{x})), \tag{3}$$

which takes the value 1 where there is neither cell nor obstacle, and 0 elsewhere (see Fig. 1a, b). The function $f_\psi(d_o(\mathbf{x})) = \mathscr{H}(d_o(\mathbf{x}) - d_o^{\text{ef}})$ locates the obstacles ($f_\psi = 0$ where an obstacle is placed, $f_\psi = 1$ elsewhere). $\mathscr{H}$ is a smoothed-out Heaviside function[1] that displays a hyperbolic tangent profile at obstacle boundaries. $d_o(\mathbf{x})$ is the distance between point $\mathbf{x}$ and its closest obstacle and $d_o^{\text{ef}} = 1.7$ μm is an effective distance for obstacle detection.

2.2 Cytosol biomechanics

Inside the cell, we consider myosin $\rho_m(\mathbf{x}, t)$ dynamics, phase transformations between G-actin $\rho_g(\mathbf{x}, t)$ and F-actin $\rho_f(\mathbf{x}, t)$, and the flow of the F-actin network, treated as a Newtonian fluid and directed by its velocity $\mathbf{u}(\mathbf{x}, t)$. Cell morphodynamics results from the force balance equation $\nabla \cdot \boldsymbol{\sigma} + \mathbf{F} = 0$, where $\boldsymbol{\sigma}$ accounts for the passive (viscous) and active (contraction and protrusion) stresses, and $\mathbf{F}$ represents the external forces applied to the cell.

The classic approach would be to solve the evolution equations on a moving domain, i.e., the cell. However, we can pose the equations on a larger and fixed domain Ω by taking advantage of the diffuse domain framework (Li et al. 2009; Teigen et al. 2009). As we explain in "Appendix A1", the inclusion of ϕ into the space and time differential operators

[1] We take $\mathscr{H}(x) = 0.5 + 0.5\tanh(7x)$ throughout this work.

imposes a zero-flux condition on the membrane and restricts dynamics to the cell's interior.

2.2.1 Myosin dynamics

Myosin dynamics is governed by a convection-diffusion equation, where molecular motors are transported by the F-actin network velocity. Simultaneously, myosin diffuses throughout the cell, giving rise to the evolution equation

$$\frac{\partial(\phi\rho_m)}{\partial t} + \nabla\cdot(\phi\rho_m\mathbf{u}) = \nabla\cdot\left[D_m(\rho_f)\phi\nabla\rho_m\right]. \tag{4}$$

The actin-dependent diffusion $D_m(\rho_f) = D_m^{\max}/(1 + K_m^2\rho_f^2)$, with $D_m^{\max}$ and K_m constant parameters, produces an effective advection towards regions of low F-actin density. This phenomenological approach accounts for the accumulation of myosin at the cell's rear, causing the tail's retraction.

2.2.2 Actin dynamics

Globular actin (ρ_g) subunits, which diffuse throughout the cell, may polymerize turning into actin filaments (ρ_f), forming an intricate network that spreads over the cell. At the same time, F-actin may disassemble recovering the G-actin state. These transformations are regulated by various signaling proteins. In addition, amoeboid cells exhibit denser actin-rich structures, i.e., the pseudopods, whose protrusive nature differs from the rest of the F-actin network. Here, we model actin dynamics using the energy functional

$$\begin{aligned}\mathscr{F}[\rho_f,\rho_g] = \int_\Omega \phi\Big[&\frac{\varepsilon_f^2}{2}|\nabla\rho_f|^2 + \frac{\varepsilon_g^2}{2}|\nabla\rho_g|^2 \\ &+ F\left(\rho_f,\rho_g,a\right)\Big]\mathrm{d}\Omega \\ &+ \lambda_N\left(N_0 - N[\rho_f,\rho_g]\right).\end{aligned} \tag{5}$$

The parameters ε_f and ε_g control the diffusive length scales of F-actin and G-actin, respectively. $N[\rho_f,\rho_g] = \int_\Omega \phi(\rho_f+\rho_g)\mathrm{d}\Omega$ is the total amount of actin within the cell, whose value at the initial time is N_0. Thus, λ_N is a Lagrange multiplier that keeps N constant throughout the cell motion. Finally, F is a function that determines the phase transitions between G-actin and F-actin in terms of the activator a (described in Sect. 2.4), expressed as

$$\begin{aligned}F\left(\rho_f,\rho_g,a\right) = {}& 10(\rho_f-\rho_f^{\mathrm{pr}})^2(\rho_f-\rho_f^{\mathrm{pa}})^2 + 7.5(\rho_g-\rho_g^{\mathrm{eq}})^2 \\ &+ I(a)(\rho_f-\rho_f^{\mathrm{pr}})^2[\rho_f+\kappa(a)I(a)].\end{aligned} \tag{6}$$

Here, the functions $I(a) = -2 + 2.6\,a$ and $\kappa(a) = a/3$ determine the dependence of F-actin stability on the activator concentration. In Eq. (6), $\rho_f^{\mathrm{pr}} = 3/2$ represents protrusive structures (i.e., the pseudopods), $\rho_f^{\mathrm{pa}} = 1/2$ is associated with a non-protrusive (passive) state of the network, and $\rho_g^{\mathrm{eq}} = 1$ represents the G-actin equilibrium density. The function F is a convex function of ρ_g, with a minimum at ρ_g^{eq}. For low activator concentrations, F is a non-convex function of ρ_f with two minima at densities ρ_f^{pa} and ρ_f^{pr}. As a increases, F transitions to a convex function of ρ_f, with a unique minimum at ρ_f^{pr}. In Fig. 1c we have plotted the function $-\partial F/\partial\rho_f$ [see Eq. (7)] for different values of a. While high values of a lead to pseudopod formation (Fig. 1c, bottom), lower values of a energetically favor the presence of passive F-actin network (Fig. 1c, top). See Moure and Gomez (2016, 2017) for more details. Actin phase transitions follow the philosophy of the wave-pinning model proposed in Mori et al. (2008). In our model, the activator represents the external stimulus that triggers cell polarization.

According to Eq. (5), a should be a compound living on the cytosol. Conceptually, in our model, a is a generic membrane-bound protein (e.g., PIP3) that triggers a set of reactions inside the cell close to the membrane. This involves the production of pro-nucleation factors a_{PNF} (e.g., Rac), which are the accessory proteins that effectively cause actin polymerization (see Fig. 1a, red dots). Thus, in the previous formulation, we should use a_{PNF} instead of a. However, we suppose that pro-nucleation factors concentrate mainly near the membrane. We further suppose that a_{PNF} is proportional to a, which allows us to use a in Eqs. (5) and (6) thanks to the diffuse domain approach.

Using the framework of non-conserved dynamics, we derive evolution equations for ρ_f and ρ_g using the functional $\mathscr{F}$. This leads to

$$\begin{aligned}\frac{\partial(\phi\rho_f)}{\partial t} + \nabla\cdot(\phi\rho_f\mathbf{u}) &= -\Gamma_f\frac{\delta\mathscr{F}}{\delta\rho_f} \\ &= \Gamma_f\left[\varepsilon_f^2\nabla\cdot(\phi\nabla\rho_f) - \phi\frac{\partial F}{\partial\rho_f} + \lambda_N\phi\right],\end{aligned} \tag{7}$$

$$\begin{aligned}\frac{\partial(\phi\rho_g)}{\partial t} + \nabla\cdot(\phi\rho_g\mathbf{u}) &= -\Gamma_g\frac{\delta\mathscr{F}}{\delta\rho_g} \\ &= \Gamma_g\left[\varepsilon_g^2\nabla\cdot(\phi\nabla\rho_g) - \phi\frac{\partial F}{\partial\rho_g} + \lambda_N\phi\right],\end{aligned} \tag{8}$$

where Γ_f is a constant and $\delta\mathscr{F}/\delta\rho_f$ is the variational derivative of the functional $\mathscr{F}$ with respect to the F-actin density. Γ_g and $\delta\mathscr{F}/\delta\rho_g$ are defined analogously. We may obtain the value of the Lagrange multiplier λ_N by forcing $\partial N/\partial t = 0$. Using the definition of N, we have $\int_\Omega \partial(\phi\rho_f)/\partial t\,\mathrm{d}\Omega + \int_\Omega \partial(\phi\rho_g)/\partial t\,\mathrm{d}\Omega = 0$. We consider either periodic or Dirichlet ($\phi = 0$) boundary conditions on $\partial\Omega$, which after the integration of Eqs. (7) and (8) lead to

$$\lambda_N = \frac{\Gamma_f\int_\Omega\phi\frac{\partial F}{\partial\rho_f}\mathrm{d}\Omega + \Gamma_g\int_\Omega\phi\frac{\partial F}{\partial\rho_g}\mathrm{d}\Omega}{(\Gamma_f+\Gamma_g)\int_\Omega\phi\mathrm{d}\Omega}. \tag{9}$$

We further assume that: (1) The Lagrange multiplier λ_N strongly forces $N = N_0 \quad \forall t$, (2) ε_g is large enough[2] to neglect the spatial variation of G-actin inside the cell, thus $\rho_g(\mathbf{x}, t) \rightarrow \rho_g(t)$. Under these hypotheses, we can obtain the value of ρ_g from the identity $N[\rho_f, \rho_g] = N_0$, as

$$\rho_g(t) = \frac{N_0 - \int_\Omega \phi \rho_f \mathrm{d}\Omega}{\int_\Omega \phi \mathrm{d}\Omega}. \tag{10}$$

Therefore, in our model, we can replace Eq. (8) by (10). Neglecting the dependence of ρ_g on space leads to a simpler and faster computational method.

2.2.3 F-actin network flow

The F-actin network is treated as a viscous fluid, whose behavior is governed by a Stokes-type equation. In addition to neglecting inertial forces,[3] we omit the pressure term following Rubinstein et al. (2009). The equation, which is augmented with forces related to the cell motion machinery (see Fig. 1a), may be written as

$$\nabla \cdot (\boldsymbol{\sigma} + \boldsymbol{\sigma}_{\mathrm{myo}} + \boldsymbol{\sigma}_{\mathrm{prot}} + \boldsymbol{\sigma}_{\mathrm{rep}}) + \mathbf{F}_{\mathrm{adh}} + \mathbf{F}_{\mathrm{mem}} = 0, \tag{11}$$

where $\boldsymbol{\sigma} = \phi[\mu(\nabla \mathbf{u} + \nabla \mathbf{u}^T) + \lambda(\nabla \cdot \mathbf{u})\mathbf{I}]$ is the classical stress tensor for a Newtonian fluid, with μ and λ the viscosity coefficients and $\mathbf{I}$ the identity tensor. Myosin produces a contraction in the F-actin network, which is modeled as the isotropic contractile stress $\boldsymbol{\sigma}_{\mathrm{myo}} = \phi \rho_m \eta_m(\rho_m)\mathbf{I}$. Pseudopod protrusion is included in the model through the stress $\boldsymbol{\sigma}_{\mathrm{prot}} = -\phi \rho_f \eta_f(\rho_f)\delta_f \nabla\phi \otimes \nabla\phi$, which is normal to the membrane and vanishes away from the cell's envelope. In both contractile and protrusive tensors, the term $\eta_i(\rho_i) = \alpha_i \overline{\eta}_i + (1-\alpha_i)\overline{\eta}_i \mathscr{H}(\rho_i - \overline{\rho}_i)$ produces greater stress in regions of higher myosin and F-actin density, respectively; where index i represents m or f. The maximum strength is defined by $\overline{\eta}_i$, and α_i is a constant. The parameters $\overline{\rho}_m = 0.9$ and $\overline{\rho}_f = (\rho_f^{\mathrm{pr}} + \rho_f^{\mathrm{pa}})/2$ establish the thresholds between low and high stresses. Finally, δ_f annihilates protrusive stresses when the cell membrane approaches an obstacle. The function δ_f is defined in "Appendix A2".

When the cell approaches an obstacle, a repulsive force acting on the membrane stops its motion. This is accomplished with the repulsive stress $\boldsymbol{\sigma}_{\mathrm{rep}} = \phi \eta_{\mathrm{rep}} \delta_{\mathrm{rep}} \nabla\phi \otimes \nabla\phi$, which is normal to the membrane and proportional to the parameter η_{rep}. The term $\delta_{\mathrm{rep}} = \mathscr{H}(d_o^{\mathrm{ef}} - d_o(\mathbf{x}))$ activates this stress only in the vicinity of the obstacle.

Adhesive forces between the cell and the environment are included through the term $\mathbf{F}_{\mathrm{adh}}$, where we take into account a continuous drag force and a set of punctual forces such that $\mathbf{F}_{\mathrm{adh}} = \mathbf{F}_{\mathrm{drag}} + \sum_j \mathbf{F}^j_{\mathrm{punct}}$. The drag force $\mathbf{F}_{\mathrm{drag}} = -\varsigma \mathbf{u}$ is proportional to F-actin velocity, with ς the drag coefficient. Each punctual adhesion j produces a punctual force $\mathbf{F}^j_{\mathrm{punct}} = -k^j_{\mathrm{grip}}(t)(\mathbf{x}^j - \mathbf{x}^j_0)\delta(\mathbf{x} - \mathbf{x}^j)$, applied on the F-actin network at point $\mathbf{x}^j$, where $\delta(\mathbf{x})$ denotes the Dirac delta function. The force is modeled as a spring with one end attached to the substrate ($\mathbf{x}^j_0$) and the other end to the F-actin network ($\mathbf{x}^j$). We include adhesion maturation (Choi et al. 2008) by proposing a time-dependent spring constant $k^j_{\mathrm{grip}}(t) = k_{\mathrm{grip}_0}(t - t^j_0)$, where k_{grip_0} is a constant and t^j_0 is the time at which adhesion j clutches. Since we consider a rigid substrate (or rigid fibers), each point $\mathbf{x}^j_0$ remains fixed. However, each point $\mathbf{x}^j$, connected to the F-actin network, moves according to the velocity $\mathbf{u}$. The procedure employed to determine punctual adhesion behavior (adhesion formation, time evolution, and rupture) is explained in "Appendix A2". In the 2D case, $\mathbf{F}^j_{\mathrm{punct}}$ and $\mathbf{F}_{\mathrm{drag}}$ play a similar role. Therefore, for the sake of simplicity, we neglect $\mathbf{F}^j_{\mathrm{punct}}$ in the 2D examples. In the 3D examples, $\mathbf{F}_{\mathrm{drag}}$ models an hydrodynamic drag between actin filaments within the cell.

The derivation of the membrane forces can be found in Moure and Gomez (2017). Starting from the Helfrich membrane energy, and taking advantage of the phase-field properties, we can define the bending and the surface tension forces in terms of the phase-field variable. As shown in Marth and Voigt (2014), bending forces can be neglected for realistic values of the parameters, and thus, the membrane forces may be expressed as $\mathbf{F}_{\mathrm{mem}} = -\gamma \nabla\phi(\varepsilon \nabla^2\phi - G'(\phi)/\varepsilon)$, where γ is the surface tension coefficient.

2.3 Extracellular chemoattractant

Chemotaxis usually originates from the presence of an extracellular substance, generally called ligand or chemoattractant, that is perceived by the cell and guides its motion. Here, we consider a single ligand $q(\mathbf{x}, t)$ that diffuses throughout the extracellular environment, experiments a natural degradation, and reacts with membrane receptors. According to the diffuse domain framework (see "Appendix A1"), the governing equation may be written as

$$\frac{\partial(\psi q)}{\partial t} = \nabla \cdot \left(D_q \psi \nabla q\right) - r_q \psi q + b_q \psi S_q - k_q \delta_m q, \tag{12}$$

where D_q, r_q, and b_q are the chemoattractant diffusion coefficient, degradation rate, and strength of the source term, respectively. The chemoattractant source is defined as $S_q = \sum_i S_i$. Here, $S_i = (q_{\max,i} - q)\delta^q_{\mathbf{x},i}\delta^q_{t,i}$ where $q_{\max,i}$ is a constant, $\delta^q_{\mathbf{x},i}$ gives the spatial location of each source i, and $\delta^q_{t,i}$ is the time localizer. $q_{\max,i}$, $\delta^q_{\mathbf{x},i}$, and $\delta^q_{t,i}$ differ depend-

[2] The large diffusion constant of G-actin has been noted in the literature; see Novak et al. (2008).

[3] For amoeboid cellular motion $\mathrm{Re} \sim 10^{-6}$.

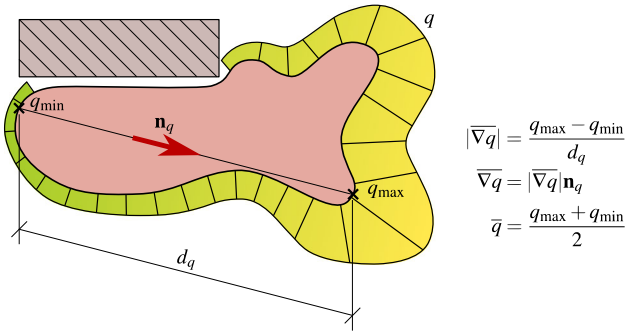

Fig. 2 Computation of the signaling parameters. $\overline{\nabla q}$ and $\overline{q}$ are established through the maximum and minimum values of chemoattractant detected by the cell along the membrane. The areas of the membrane that are in contact with a solid obstacle are not considered to compute $\overline{\nabla q}$ and $\overline{q}$

ing on each example[4] and we only consider one chemotactic source active at the same time. We model the ligand-receptor interaction as a consumption proportional to the ligand concentration at the membrane, with rate k_q.

A cell is able to sense extracellular signals through the membrane, in particular, through membrane receptors. The ligand binds to the receptors. The receptors change from inactive to active (see Fig. 1a), at a rate depending on the ligand concentration at the cell surface (Swaney et al. 2010). Variations in the receptor occupancy along the membrane determine the direction of the signal to the cytosolic machinery to a significant extent, but also the average level of occupancy may affect the signaling transduction [e.g., receptor saturation is a consequence of a finite number of receptors (Song et al. 2006)]. Here, we assume that the number of bound receptors is proportional to the chemoattractant density along the membrane (Levine et al. 2006). Based on the previous arguments, we suppose that chemotactic motion is controlled by the *signaling parameters* $\overline{\nabla q}$ and $\overline{q}$, which represent an average chemoattractant gradient and the mean chemoattractant concentration. To define $\overline{\nabla q}$ and $\overline{q}$, we consider the distribution of chemoattractant concentration q along the membrane (see Fig. 2). Let us denote $q_{\min}$ and $q_{\max}$ the minimum and maximum values of q along the membrane. $\mathbf{n}_q$ is a unit vector parallel to the line that joins the points where the values $q_{\min}$ and $q_{\max}$ are attained. We define $|\overline{\nabla q}| = (q_{\max} - q_{\min})/d_q$, where d_q is the distance between the membrane points with minimum and maximum chemoattractant concentration. The vector $\overline{\nabla q}$ is defined as $\overline{\nabla q} = |\overline{\nabla q}|\mathbf{n}_q$. The average chemoattractant concentration is defined as $\overline{q} = (q_{\max} + q_{\min})/2$. As indicated in Fig. 2, we suppose that when the cell touches an obstacle, the ligand does not interact with the membrane in the contact region.

[4] In this work, we suppose spherical (circular in 2D) chemoattractant sources. Thus, $\delta^q_{\mathbf{x},i} = \mathscr{H}(R_q - d^q_i(\mathbf{x}))$, where $R_q = 1\ \mu\text{m}$ and $d^q_i(\mathbf{x})$ denotes the distance from point $\mathbf{x}$ to the center of source i.

2.4 Membrane activator

Membrane-bound signaling molecules such as, e.g., PIP3, trigger the polymerization of actin filaments. Our model considers one single compound called activator $a(\mathbf{x}, t)$, which produces actin nucleation. In the formulation, this can be understood by examining the actin energy functional $\mathscr{F}$ [see Sect. 2.2.2, Eqs. (5) and (6)]. We make use again of the diffuse domain method (see "Appendix A1") to derive an evolution equation for the activator. We propose the model

$$\frac{\partial(\delta_m a)}{\partial t} + \nabla\cdot(\delta_m a\mathbf{u}) = \nabla\cdot(D_a\delta_m\nabla a) - r_a\delta_m a + b_a\delta_m S_a, \tag{13}$$

which accounts for advection and diffusion throughout the membrane, with diffusion constant D_a. In addition, we consider a natural decay with rate r_a and a growth term S_a that produces peaks of activator, with a strength set by the parameter b_a. The source term $S_a = (a_{\max} - a)\sum_i \delta^a_{\mathbf{x},i}\delta^a_{t,i}$ drives a to $a_{\max} = 1.5$ at certain regions (defined by $\delta^a_{\mathbf{x},i}$) and interval times (defined by $\delta^a_{t,i}$), producing peaks in the activator concentration and eventually the emergence of pseudopods. Therefore, pseudopod formation is controlled by $\delta^a_{\mathbf{x},i}$ and $\delta^a_{t,i}$, which are calculated through probability functions taken from experimental works (Bosgraaf and Van Haastert 2009a, b; Van Haastert 2010; Fuller et al. 2010); see Fig. 3. The functions $\delta^a_{\mathbf{x},i}$ and $\delta^a_{t,i}$ are smoothed-out step functions that depend on parameters that define the spatio-temporal location of the activator peaks. Since we follow the pseudopod-centered view (Insall 2010), we first calculate the parameters as if the cell was undergoing spontaneous motion (no chemotaxis) and then modify them using a chemotactic bias. The relevant parameters are the location of the i-th activator peak $\mathbf{s}^*_i$ (used for the spatial localizer $\delta^a_{\mathbf{x},i}$), the time between two consecutive peaks $\Delta\tau^*_i$ (called interval and used to define $\delta^a_{t,i}$), and the growth time of the peak ΔT^*_i (also used in $\delta^a_{t,i}$). Note that we use an asterisk to denote the parameters for spontaneous motion. The values of $\mathbf{s}^*_i$, $\Delta\tau^*_i$, and ΔT^*_i are obtained using the probability functions shown in Fig. 3a which are taken from experiments. Note that, for consistency with the previous section, we preclude pseudopod formation in regions of cell-obstacle contact. More details on the definition of $\mathbf{s}^*_i$, $\Delta\tau^*_i$, and ΔT^*_i for two- and three-dimensional problems may be found in "Appendix A2"; see also Moure and Gomez (2017).

Once the spontaneous motion parameters ($\mathbf{s}^*_i$, $\Delta\tau^*_i$, and ΔT^*_i) have been obtained, we modify them using the signaling parameters $\overline{\nabla q}$ and $\overline{q}$ to obtain $\mathbf{s}_i$, $\Delta\tau_i$, and ΔT_i. The first step in the process is to compute the bias $\beta \in [0, 1]$ using ideas from the stochastic model from Van Haastert (2010). We apply the multiplicative split $\beta = \beta_{\overline{\nabla q}}\beta_{\overline{q}}$ to isolate the effect of the two control parameters that determine the

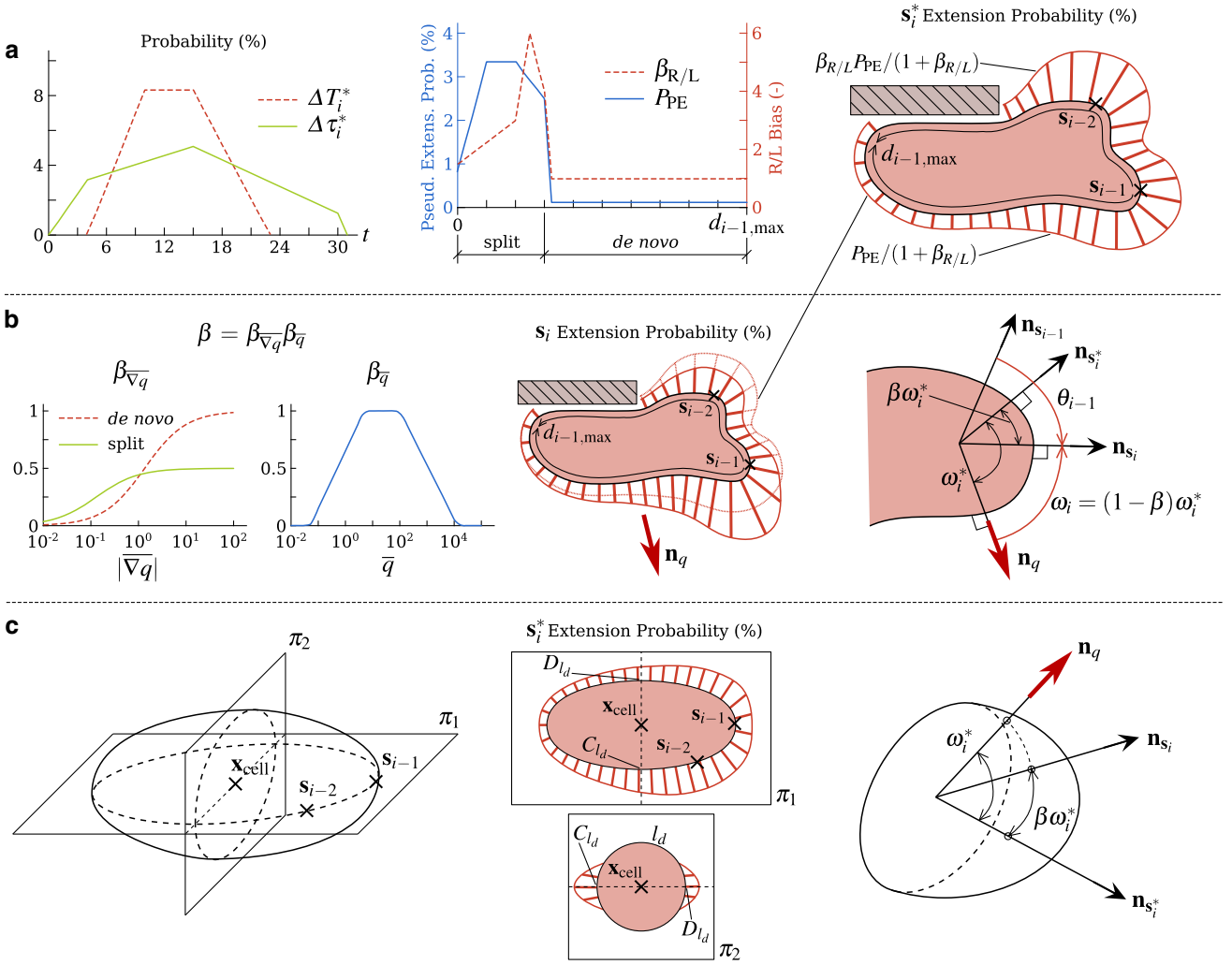

Fig. 3 Determination of pseudopod formation. **a** Growth time (ΔT_i^*), interval ($\Delta \tau_i^*$), pseudopod extension (P_{PE}), and right–left bias ($\beta_{R/L}$) probability distributions, derived from Bosgraaf and Van Haastert (2009b). Probability distribution of $\mathbf{s}_i^*$ given the locations $\mathbf{s}_{i-1}$ and $\mathbf{s}_{i-2}$ in a 2D computation. **b** Chemotactic bias (β) produced by the gradient ($\beta_{\overline{\nabla q}}$) and the average level ($\beta_{\overline{q}}$) of chemoattractant, derived from Song et al. (2006); Fuller et al. (2010); Van Haastert (2010). Probability distribution of $\mathbf{s}_i$ modified by β and the gradient direction $\mathbf{n}_q$. Diagram showing how $\mathbf{n}_{\mathbf{s}_i^*}$ is rotated to determine ω_i and $\mathbf{s}_i$. **c** The process to determine $\mathbf{s}_i$ can be extended to 3D by proceeding analogously to the 2D case on the plane defined by $\mathbf{n}_q$ and $\mathbf{n}_{\mathbf{s}_i^*}$

strength of the chemotactic bias. The value of $\beta_{\overline{\nabla q}}$ depends on whether the pseudopod is a split or *de novo*; see Fig. 3b (left) where the value of $\beta_{\overline{\nabla q}}$ approximates the values given by Van Haastert (2010). The value of $\beta_{\overline{q}}$ is also plotted on the left-hand side of Fig. 3b and follows the data of Song et al. (2006) and Fuller et al. (2010). Let us call $\mathbf{n}_{\mathbf{s}_i^*}$ the normal vector to the membrane at point $\mathbf{s}_i^*$; see the right-hand side of Fig. 3b. The angle between the vectors $\mathbf{n}_q$ and $\mathbf{n}_{\mathbf{s}_i^*}$ is denoted ω_i^*. The point $\mathbf{s}_i$ is located in the neighborhood of $\mathbf{s}_i^*$ such that the angle between $\mathbf{n}_q$ and $\mathbf{n}_{\mathbf{s}_i}$ is as close as possible to $\omega_i = (1-\beta)\omega_i^*$. This idea can be extended to 3D migration as illustrated on the left-hand side of Fig. 3c; more details in "Appendix A2". According to Bosgraaf and Van Haastert (2009a), the time interval between two consecutive pseudopods is not affected by chemotaxis, that is, $\Delta\tau_i = \Delta\tau_i^*$. However, the life time of pseudopods is greater if they point in the same direction as $\mathbf{n}_q$. We describe this quantitatively using the formula $\Delta T_i = \Delta T_i^*[1 + 0.1\cos(\omega_i)]$.

3 Numerical method

We consider a fixed set Ω that represents our computational domain. The boundary of Ω is Γ. To simulate the cell motion problem, we need to solve Eqs. (1), (4), (7), (11), (12), and (13) on the domain Ω and a time interval of interest. We assume that the unknowns ϕ, ρ_m, ρ_f, and a vanish on the boundary Γ. We also assume stress-free and flux-free con-

ditions on Γ. Mathematically, these can be expressed as $(\boldsymbol{\sigma} + \boldsymbol{\sigma}_{\text{myo}} + \boldsymbol{\sigma}_{\text{prot}} + \boldsymbol{\sigma}_{\text{rep}})\,\mathbf{n}_\Gamma = 0$ and $\nabla q \cdot \mathbf{n}_\Gamma = 0$, respectively. Here, $\mathbf{n}_\Gamma$ is the unit outward normal vector on Γ. Note that Eqs. (9) and (10) are also necessary to solve the cell-motion problem, but they do not need to be discretized. Therefore, we do not consider them in this section.

3.1 Weak form and spatial discretization

To solve the equations numerically, we will use isogeometric analysis, a spline-based finite element method (Hughes et al. 2005). We begin by deriving a weak form of the equations by multiplying them with weighting functions, integrating over the computational domain, and integrating by parts; see Eqs. (21)–(26) in "Appendix A3" for more details.

By examining the weak form, it may be observed that a conforming discretization requires basis functions which are at least $\mathscr{C}^1$-continuous across element boundaries. This can be easily achieved using isogeometric analysis. The Galerkin form can be derived by replacing in the weak form the unknowns and the weighting functions with discrete approximations. Further details on the spatial discretization may be found in "Appendix A3" and Moure and Gomez (2017).

3.2 Time-stepping scheme and numerical implementation

We employ a semi-implicit time integration scheme based on the generalized-α method (Chung and Hulbert 1993; Jansen et al. 2000). All the terms of the residual are treated implicitly, except those which require non-local computations, such as, for example, calculating integrals or distances. In particular, we treat explicitly the terms λ_N, ρ_g, and δ_{rep}. The resulting non-linear system is solved using the Newton–Raphson method. We also use a simple adaptive time stepping scheme in which the time step size is modified based on the convergence of the Newton–Raphson solver. When the convergence is slow, the algorithm reduces the time step size for a given time interval. When the convergence is fast, the time step is slowly increased. Further details on the numerical implementation can be found in "Appendix A3".

4 Results and discussion

In this section, we show the ability of our method to reproduce amoeboid chemotactic motion. We present several 2D and 3D computations. For a particular initial cell geometry, given by the function $\phi(\mathbf{x}, 0)$, the cytosolic components are initialized in all examples as $\rho_m(\mathbf{x}, 0) = \phi(\mathbf{x}, 0)$, $\rho_f(\mathbf{x}, 0) = \rho_f^{\text{pa}}\phi(\mathbf{x}, 0)$, and $\rho_g(\mathbf{x}, 0) = \alpha_g\phi(\mathbf{x}, 0)$ with $\alpha_g = 1.1$ in the 2D examples and $\alpha_g = 0.9$ in the 3D computations. The chemoattractant and activator concentrations as well as the velocity are assumed to vanish at the initial time in all examples. Note that, cell morphodynamics (including average cell volume) results from the balance between myosin-induced contraction and actin protrusion. Because the mass of actin and myosin is conserved in the model, the balance is determined by the initial conditions. Strong variations in the initial conditions may lead to unrealistic results. The parameter values used in the simulations may be found in "Appendix A4".

4.1 Analysis of chemotactic motion

We initially analyze the behavior of cells under different chemotactic conditions neglecting the chemoattractant dynamics. Thus, we disregard Eq. (12) and assume that $|\overline{\nabla q}|$, $\overline{q}$, and $\mathbf{n}_q$ are constants imposed *a priori*. We will take $\mathbf{n}_q = \{1, 0\}^T$ in all simulations and vary $|\overline{\nabla q}|$ and $\overline{q}$. To study chemotaxis in large environments without employing unaffordable computational domains, we resort to periodic boundary conditions. We use a 2D computational domain $\overline{\Omega} = [-L, L]^2$ with $L = 25$ μm. The domain is discretized using 200 $\mathscr{C}^1$-continuous quadratic elements in each direction. We take an initial time step $\Delta t = 0.05$ s. The initial cell geometry is given by a circle[5] of radius $R_c = 8$ μm centered at the origin of coordinates.

First, we analyze the influence of $|\overline{\nabla q}|$. Thus, we keep constant $\overline{q} = 80$ nM and perform 10 independent simulations for each value of $|\overline{\nabla q}|$. We study the interval $[0, T]$, where $T = 15$ min. We consider three values of $|\overline{\nabla q}|$, namely 0.1, 1, and 10 nM/μm. The results are plotted in Fig. 4, where each column corresponds to a value of $|\overline{\nabla q}|$, increasing from left to right. Figure 4a shows the tracks of the cells. As $|\overline{\nabla q}|$ increases, the cells lose their characteristic persistent random motion and exhibit a movement guided by $\mathbf{n}_q$. We define the chemotactic index CI as the displacement in the gradient direction over the total distance traveled in the simulation.[6] The average CI over the cell population increases with $|\overline{\nabla q}|$, as shown in the plot. Figure 4b shows the frequency histogram of the angle ω_i (red bars) and the average pseudopod size (blue crosses) as a function of ω_i. The angle ω_i has been measured as shown in Fig. 3b (right) and pseudopod size has been estimated as the net distance traveled by $\mathbf{s}_i$ during its growth time ΔT_i. The histogram of ω_i is approximately symmetric, with the highest frequencies concentrating around $\omega_i \sim 0°$ as $|\overline{\nabla q}|$ increases. For exam-

[5] Due to the use of the phase-field method, a circular cell is described using a smooth function given by $\phi(\mathbf{x}, 0) = 0.5 - 0.5\tanh[\frac{2\sqrt{2}}{\varepsilon}(d_c(\mathbf{x}) - R_c)]$, where $d_c(\mathbf{x})$ is the distance to the center of the cell. Similar initial conditions based on hyperbolic tangents will be used throughout the paper.

[6] More precisely, $CI = d_{\mathbf{n}_q}/d_{\text{cell}}$, where $d_{\mathbf{n}_q} = \int_0^T \mathbf{u}_{\text{cell}} \cdot \mathbf{n}_q \,\mathrm{d}t$ and $d_{\text{cell}} = \int_0^T |\mathbf{u}_{\text{cell}}|\,\mathrm{d}t$, with $\mathbf{u}_{\text{cell}}$ the velocity of the mass center of the cell.

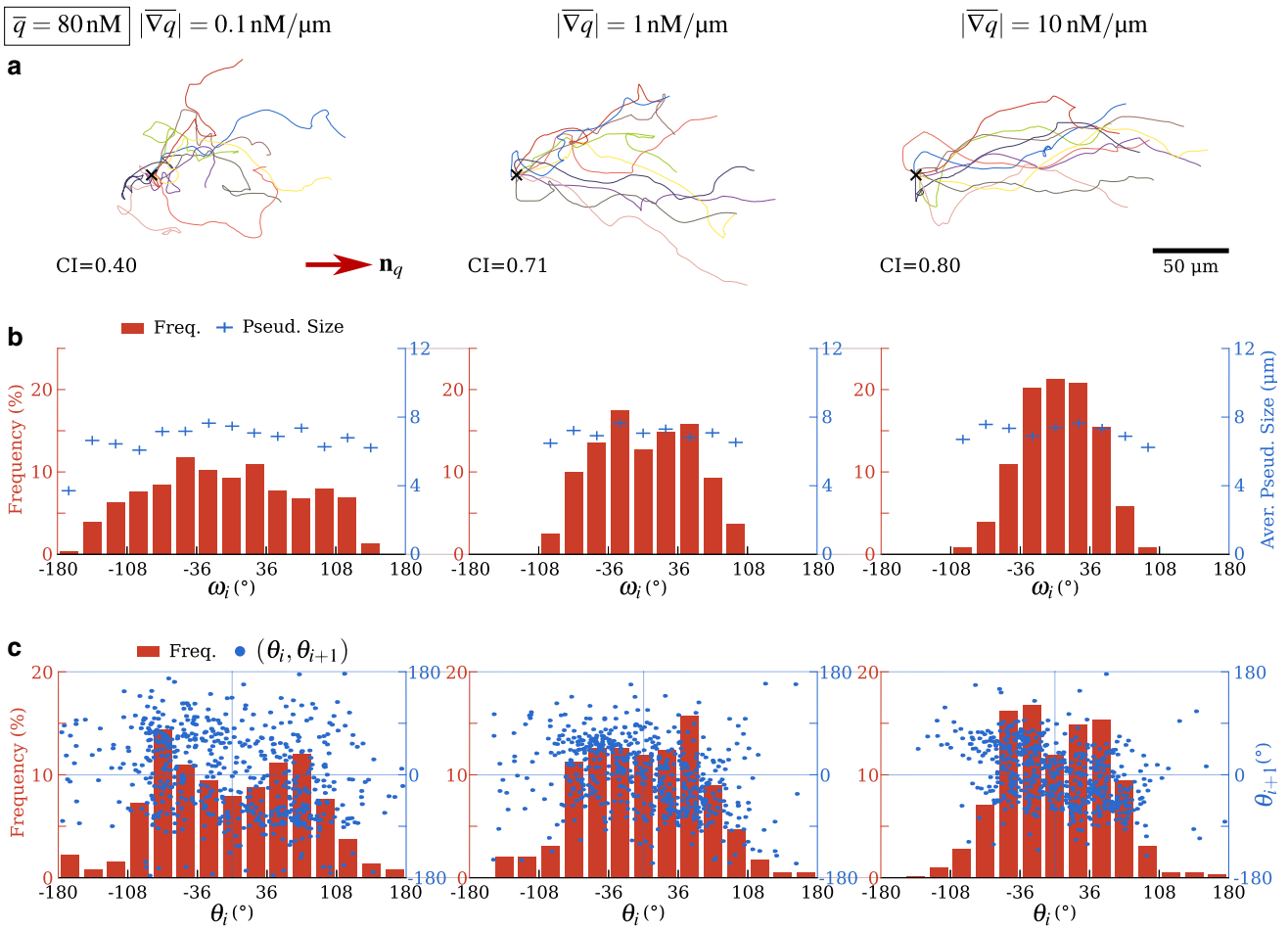

Fig. 4 Analysis of chemotactic motion. Influence of $|\overline{\nabla q}|$. Results corresponding to $|\overline{\nabla q}| = 0.1$ nM/μm (left column), $|\overline{\nabla q}| = 1$ nM/μm (middle column), and $|\overline{\nabla q}| = 10$ nM/μm (right column); with $\overline{q} = 80$ nM for all cases. **a** Tracks of the cells and chemotactic index (CI). **b** Frequency histogram of ω_i and average pseudopod size as a function of ω_i. **c** Frequency histogram of θ_i and distribution of the pairs (θ_i, θ_{i+1}). See Fig. 3b for a description of angles ω_i and θ_i

ple, for $|\overline{\nabla q}| = 0.1$ μM/μm the histogram spreads almost over the entire range of ω_i, namely $[-180°, 180°]$, but for $|\overline{\nabla q}| = 10$ μM/μm all the non-zero frequencies fall into the interval $[-108°, 108°]$. Pseudopod size is fairly independent of ω_i, though it displays a slight increase in the neighborhood of $\omega_i = 0°$ (Bosgraaf and Van Haastert 2009a).

To further analyze the chemotactic motion, we study the angles between consecutive pseudopods. We use θ_i, which is the angle between $\mathbf{n}_{\mathbf{s}_i}$ and $\mathbf{n}_{\mathbf{s}_{i+1}}$ (see Fig. 3b, right), as a measure of the angle between pseudopods. Figure 4c shows the frequency histogram of θ_i (red bars) as well as the distribution of the pairs (θ_i, θ_{i+1}) on a two-dimensional space (blue dots). In non-chemotactic amoeboid motion, the histogram of θ_i usually presents a symmetric distribution with respect to $\theta_i = 0°$ with two peaks around $\theta_i = \pm 55°$, while the plot of the pairs (θ_i, θ_{i+1}) is denser in the top-left- and bottom-right quadrants (Bosgraaf and Van Haastert 2009b). In chemotactic motion, the histogram of θ_i remains approximately symmetric, but the two peaks are closer to $\theta_i = 0°$ as $|\overline{\nabla q}|$ increases. The distribution of the pairs (θ_i, θ_{i+1}) is still denser on the top-left and bottom-right quadrants, but is more populated in the region that corresponds to smaller angles. Note that, once the cell is moving in the direction of $\mathbf{n}_q$, the probability distribution of pseudopod extension affected by the chemotactic bias displays very low values at the back and the sides of the cell. These values are lower as $|\overline{\nabla q}|$ increases. This is the reason why it is difficult to observe abrupt changes in the cell direction, i.e., angles θ_i close to $-180°$ and $180°$, for high values of $|\overline{\nabla q}|$; see Fig. 4c (right).

The influence of $\overline{q}$ on chemotactic cell motility is studied through ten independent simulations with a 15-minute duration. We take $|\overline{\nabla q}| = 1$ nM/μm for all simulations and analyze the cases given by $\overline{q} = 80$, 800, and 8000 nM. Figure 5 shows the results using the same format as in the previous figure. Notably, the results show that the chemotactic index CI decreases as we increase $\overline{q}$. This is a phenomenon

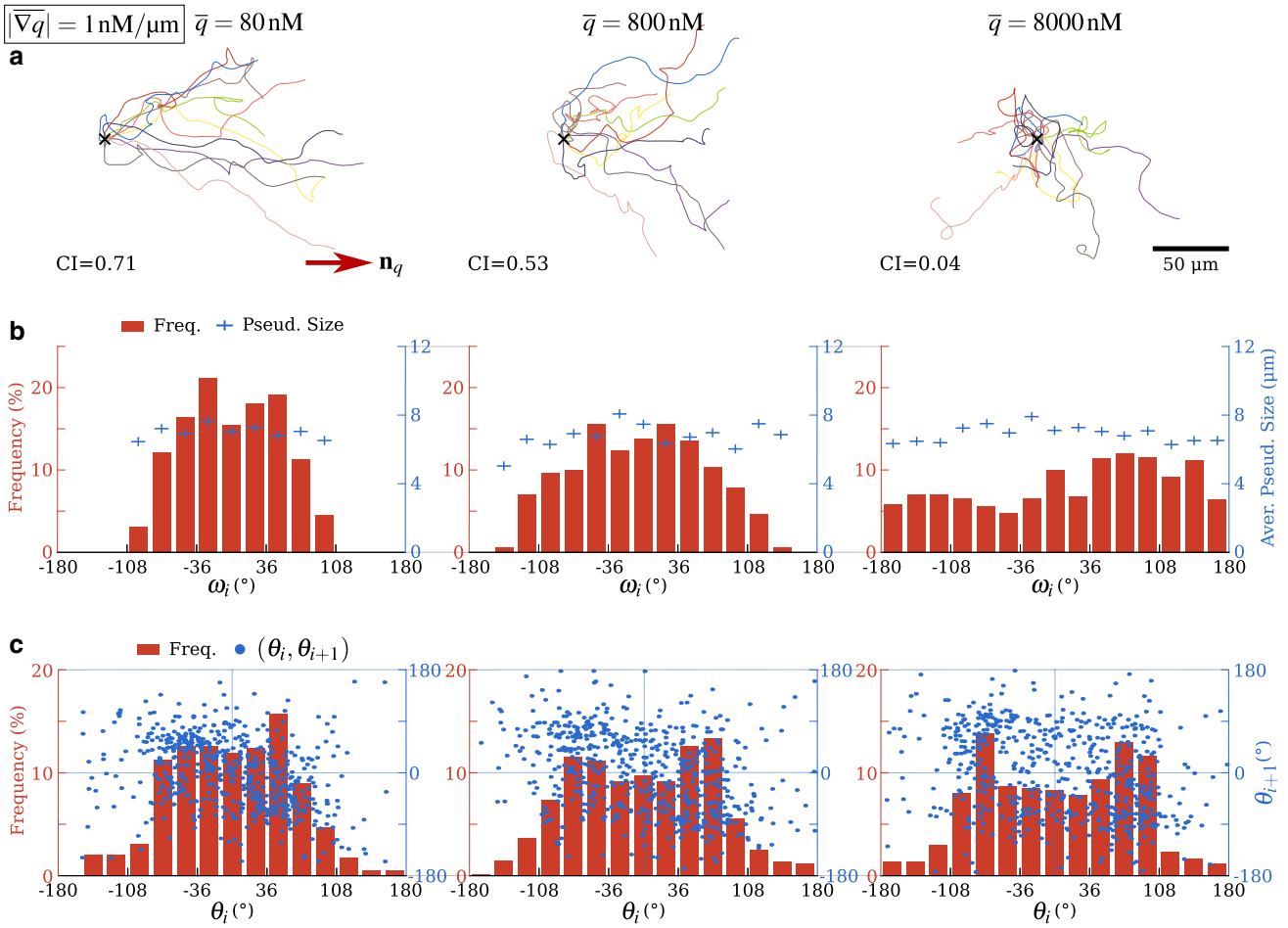

Fig. 5 Analysis of chemotactic motion. Influence of $\overline{q}$. Results corresponding to $\overline{q} = 80$ nM (left column), $\overline{q} = 800$ nM (middle column), and $\overline{q} = 8000$ nM (right column); with $|\overline{\nabla q}| = 1\,\mathrm{nM}/\mu\mathrm{m}$ for all cases. **a** Tracks of the cells and chemotactic index (CI). **b** Frequency histogram of ω_i and average pseudopod size as a function of ω_i. **c** Frequency histogram of θ_i and distribution of the pairs (θ_i, θ_{i+1}). See Fig. 3b for a description of angles ω_i and θ_i

that has also been observed experimentally. It is thought to be a consequence of receptor saturation (Song et al. 2006). Cells have a finite number of receptors. If the extracellular ligand concentration is high, most of them will be bound and the cell will find it difficult to establish differences in the level of receptor occupancy. The same argument applies for low values of $\overline{q}$; with a small amount of bound receptors the cell can not distinguish variations in occupancy along the membrane[7] (Fuller et al. 2010). Figure 5b shows that the histogram of ω_i becomes more and more uniform as $\overline{q}$ increases. In Fig. 5c, the histogram of θ_i features two symmetric peaks for all values of $\overline{q}$, which are located approximately at $\theta_i = \pm 55°$ for the largest value of $\overline{q}$, showing again a feature of non-chemotactic motion. The distribution of the pairs (θ_i, θ_{i+1}) for a given chemotactic index is consistent with experimental observations and the data presented in Fig. 4.

4.2 *Dictyostelium* aggregation mediated by natural waves

Social *Dictyostelium discoideum*, after nutrient deprivation, may experience a process called aggregation. During aggregation, cells come together guided by a signaling molecule called cAMP, secreted by the cells themselves. Individual cells located far from the aggregation center move under the influence of traveling waves of cAMP. These waves are released with a period $T_w \sim 6$ min and travel outward from the aggregation center without significant dissipation. Although cAMP waves are symmetric, cells are able to produce effective migration towards the wave source. This is known as the back-of-the-wave problem: even though the gradient reverses in the back half of the wave, cells

[7] We checked that the model also reproduces this experimental observation (data not shown).

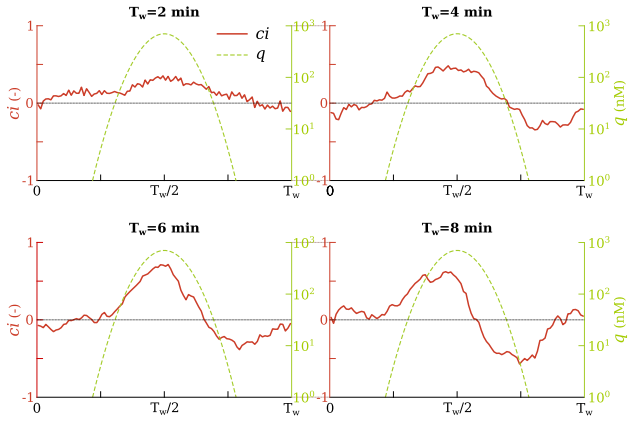

Fig. 6 *Dictyostelium* aggregation mediated by natural waves. Temporal evolution of the average instantaneous chemotactic index (ci) and cAMP concentration (q) for different values of the wave period T_w

do not exhibit effective migration away from the aggregation center. This behavior may be explained through the concept of adaptation: cells respond better to increases of chemoattractant concentration. When the chemoattractant concentration decreases, the chemotactic response diminishes (Van Haastert and Devreotes 2004). Thus, when cells encounter the cAMP wave, although the gradient strength is the same in both halves of the wave, the chemotactic response is weaker in the back half because the chemoattractant concentration decreases. It has been suggested, see, e.g., Goldstein (1996), that adaptation features a characteristic time, identified as the time the cell needs to recover its initial state of chemotactic response. Adaptation may be also thought of as a long-term memory with characteristic time scale similar to the adaptation time. The chemotactic long-term memory plays a similar role to that of the persistence time in spontaneous (non-chemotactic) *Dictyostelium* migration; i.e., maintaining the direction of the motion for a certain time. Skoge et al. (2014) explains the process of aggregation assuming that the adaptation time is similar to the period of the cAMP wave. Their experiments show that waves with greater period than the adaptation time produce reverse motion in the cell population. Our model does not include adaptation explicitly, but we show that the persistence of the motion alone enables an effective aggregation process for cAMP waves of up to ~ 6 min.

To replicate the nondissipating waves of the experiments in Skoge et al. (2014), we ignore the chemoattractant dynamics (as done in Sect. 4.1) and simply impose *a priori* a distribution $q(\mathbf{x}, t)$ that represents the traveling waves used in the experiments; see "Appendix A5" for more details. To reduce the computational time, we use a rather small computational domain, $\overline{\Omega} = [-L, L]^2$ with $L = 25$ μm, but assume periodic boundary conditions in all directions. We perform 5 independent simulations of duration $6T_w$ for each wave period $T_w = 2$, 4, 6, and 8 min. To analyze the results, we define the instantaneous chemotactic index $ci(t) = \mathbf{u}_{\text{cell}}(t) \cdot \mathbf{n}_q / |\mathbf{u}_{\text{cell}}(t)|$. Here, $\mathbf{u}_{\text{cell}}(t)$ is the velocity of the cell's center of mass. We assume that the aggregation center is located at the point $(\infty, 0)$. Thus, we expect chemotactic motion along the horizontal direction and we take $\mathbf{n}_q = \{1, 0\}^T$. Figure 6 shows the time evolution of the instantaneous chemotactic index (red line) and the cAMP concentration (dashed green line). The reported value of $ci(t)$ is the average of the 30 periods that we computed (5 simulations, with duration $6T_w$). The results show that for short periods ($T_w \sim 2$ min) the cell always moves toward the aggregation center, that is, $ci(t) > 0$ for all t. As T_w increases, $ci(t)$ attains negative values, which indicates reverse migration at the back half of the wave. For the largest period, $T_w = 8$ min, the positive and negative peaks of $ci(t)$ reach similar values and the net motion of the cell toward the aggregation center is small. Our results are in agreement with the experiments reported in Skoge et al. (2014) although the efficiency of the aggregation process deteriorates earlier in our simulations. This suggests that the time scale of the adaptation process is larger than the persistence time. In Sect. 4.7 we discuss how to incorporate adaptation into our model to obtain better quantitative agreement with the experiments of cAMP traveling waves.

4.3 Chemotactic migration on a planar surface

Here, we aim at illustrating the behavior of a cell moving along a chemoattractant gradient as well as the cell-chemoattractant interaction. Thus, this example, in contrast with those analyzed so far, considers the dynamics of the extracellular ligand described by Eq. (12). The simulation will show how a cell follows a moving chemoattractant source as observed in experiments (Swanson and Taylor 1982; Andrew and Insall 2007). We perform a simulation with duration 25 min on a 2D computational domain $\overline{\Omega} = [0, L]^2$, where $L = 100$ μm. The source term S_q in Eq. (12) is defined as $S_q = \sum_{i=1}^{5} S_i$. The source term S_i is a Gaussian function in space centered at point $\mathbf{S}_i^c$ and is non-zero in a particular time interval only. The centers are given by $\mathbf{S}_1^c = (50, 97)$, $\mathbf{S}_2^c = (97, 3)$, $\mathbf{S}_3^c = (3, 97)$, $\mathbf{S}_4^c = (50, 3)$, and $\mathbf{S}_5^c = (97, 97)$ μm; see Fig. 7. The different sources S_i with $i = 1, \ldots, 5$ are active, respectively, in the time intervals (0, 300), (300, 600), (600, 900), (900, 1200), and (1200, 1500) s. The main panel in Fig. 7 shows the entire computational domain and the numerical solution at time $t = 513$ s. The cell's interior shows the F-actin density and the membrane displays the activator concentration. Outside the cell, the color corresponds to the chemoattractant concentration. The plot also includes three rectangular insets that show the cell's location, shape and biochemical state (ρ_f and a) at different times ($t = 104$, 1012, and 1500 s). The insets also show the chemoattractant

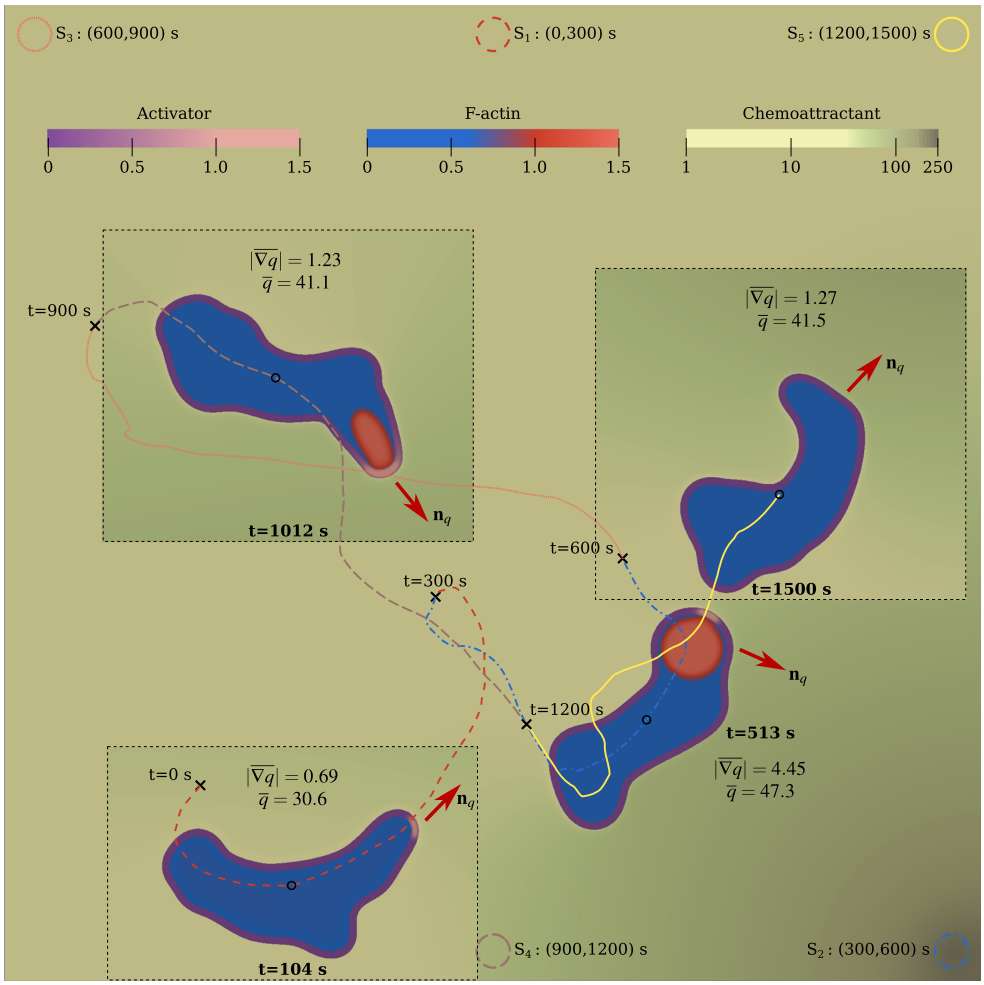

Fig. 7 Chemotactic migration on a planar surface. Activator, F-actin, and chemoattractant distributions. Simulation performed on a mesh composed of 400 $\mathscr{C}^1$-continuous quadratic elements in each direction. The initial time step is $\Delta t = 0.05$ s. The cell is initially centered at the point (20, 20) μm with a circular geometry of radius $R_c = 8$ μm. We set $D_q = 500\ \mu\text{m}^2\text{s}^{-1}$ and $q_{\max,i} = 250$ nM for $i = 1, \ldots, 5$. The main panel shows the distributions of a, ρ_f, and q at $t = 513$ s. The three insets show the distributions of a, ρ_f, and q in the neighborhood of the cell at $t = 104$, 1012, and 1500 s. The circles close to the domain boundary represent the spatial location of the chemotactic sources (S_1, S_2, S_3, S_4, and S_5), along with the interval time they are active. The cell's path is divided into five segments according to the active source. The division points are marked with crosses. $\mathbf{n}_q$ (red arrow), $|\overline{\nabla q}|$, and $\overline{q}$ (units nM/μm and nM, respectively) are indicated for the considered times $t = 104$, 513, 1012, and 1500 s. The position of the cell's center of mass is marked with a small circle

concentration in a small rectangular region of the domain around the cell. The main panel also shows the path followed by the cell's center of mass over the entire simulation. The path is divided into 5 sections represented by different line types. The section changes when the active source changes. The figure shows the section changes with crosses in the path line as well as the location of each S_i and its interval of activity. For each time, the plot shows the cell's center of mass with a small circle as well as the values of $|\overline{\nabla q}|$, $\overline{q}$, and the chemotactic direction $\mathbf{n}_q$ (red arrow). Figure 7 shows the main features of our amoeboid motion model: the membrane-bound activator triggers the emergence of pseudopods (regions of high F-actin density; see $t = 513$ and 1012 s) that push forward the membrane producing the cell motion. In this example, the signaling parameters detected by the cell display a range of values ($|\overline{\nabla q}| \sim 1$ nM/μm and $\overline{q} \sim 40$ nM) that strongly bias the movement of the cell. The cell carries out a well-directed migration towards the chemoattractant source that is active at each time, with the exception of the interval (400, 600) s. During the interval (400, 600) s, the cell actually moves in the opposite direction to $\mathbf{n}_q$, highlighting the chaotic nature of cell motion observed in experiments (e.g., Tweedy et al. 2013). Even a strong chemoattractant gradient cannot guarantee a rapid and straight displacement towards the source. In Fig. 7 we can also observe the interaction between the cell and the chemoattractant. The chemoattractant undergoes reactions with the membrane receptors and does not diffuse through the cell,

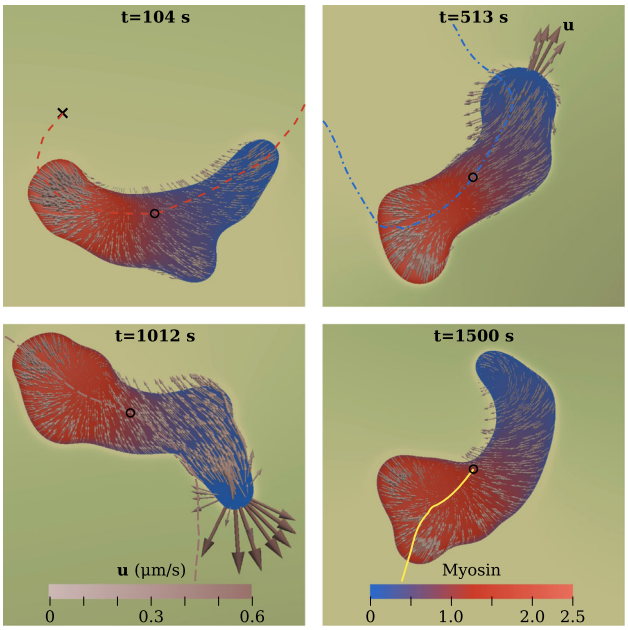

Fig. 8 Chemotactic migration on a planar surface. Myosin distribution and F-actin network velocity (grey arrows) at the same times as shown in Fig. 7 ($t = 104$, 513, 1012, and 1500 s). The chemoattractant concentration outside the cell is plotted using the same color scale as in Fig. 7

which produces a small track of low chemoattractant density behind the cell (slightly visible, e.g., at $t = 1012$ s). Figure 8 shows the myosin distribution inside the cell at times $t = 104, 513, 1012$, and 1500 s. For simplicity, we only show a small region of the computational domain at each time. In Fig. 8 we also show the F-actin velocity $\mathbf{u}$ inside the cell, represented by arrows distributed at random points. All the snapshots show the accumulation of myosin at the back of the cell, causing its retraction. However, at times $t = 104$ and 1500 s, one cannot appreciate significant protrusive velocities because there are no pseudopods pushing the membrane at those times; c.f. with Fig. 7.

4.4 Maze solving by chemotactic migration

We study chemotactic migration on a planar surface with rigid obstacles. The obstacle layout is intricate, so that the cell essentially has to migrate in a maze-like environment. The computational domain is a square of side 100 μm. The chemoattractant source is a Gaussian function located at the center of the domain and active throughout the entire time span of the simulation. Figure 9 shows the simulation results using the same format as in Fig. 7. The main panel displays the results at time $t = 370$ s, with the color outside the cell indicating the chemoattractant concentration. The color scales inside the cell and the membrane represent, respectively, F-actin density and activator concentration. There is also a yellow line showing the path followed by the cell's center of mass throughout the simulation. The black crosses on the track indicate the location of the cell's center of mass at times $t = 0$, 200, 400, 600, and 800 s. The rectangular insets marked with dashed black line show the cell's location and biochemical state as well as the chemoattractant concentration is a small region around the cell at times $t = 238$, 576, and 723 s. The plot shows that at early times ($t < 200$ s) the cell performs an inefficient migration around its initial position. The initial motion is inefficient mainly for two reasons: First, the chemotactic source is located at a large effective distance to the cell because the chemoattractant cannot penetrate the obstacles. This produces low chemoattractant gradients in the neighborhood of the cell. Second, and foremost, the chemoattractant approaches the cell from two opposite sides—left and right. As a consequence, the point of the membrane where $q_{\max}$ is located is on the left or right side of the cell, but $q_{\min}$ is attained somewhere else than left or right. Thus, the direction of $\mathbf{n}_q$, which is a unit vector pointing from $q_{\min}$ to $q_{\max}$, is not horizontal and the cell moves neither right nor left which are the two only ways out. After $t \sim 200$ s, the cell migrates towards the chemotactic source following a nearly optimal path. In particular, as the cell approaches the chemotactic source, the value of $|\overline{\nabla q}|$ becomes greater, increasing the efficiency of the motion. The strong interaction between the cell and the chemoattractant is apparent in Fig. 9. The chemoattractant binds to the cell's receptors, so that the membrane acts as a chemoattractant sink. As the same time, the extracellular ligand cannot penetrate the cell. The results clearly show that the obstacles have a strong impact on the cell motion directly, but also through the chemoattractant distribution. This is particularly visible in the insets that correspond to $t = 576$ s and $t = 723$ s. At $t = 576$ s, the chemoattractant concentration at the back of the cell is significantly lower than at the front. This happens because the boundary on the left and the obstacle on the right block chemoattractant flow producing a much higher gradient than what would be attained in obstacle-free motion. Thus, our results suggest that the presence of obstacles increases the efficiency of chemotactic migration.

In Fig. 10 we have plotted the F-actin network velocity at $t = 723$ s. To gain insight into the cell-obstacle interaction, we have also plotted the regions where protrusive stresses vanish (dashed stripes) and repulsive forces are activated (solid grey). Those regions are determined through the terms δ_f and δ_{rep}; see Sect. 2.2.3. In Fig. 10, the grey regions are enclosed by the striped ones. Therefore, when the cell approaches the obstacle, protrusive stresses are suppressed before repulsive stresses appear on the membrane. In fact, we can observe in the striped region the protrusive velocity vanishing on the membrane.

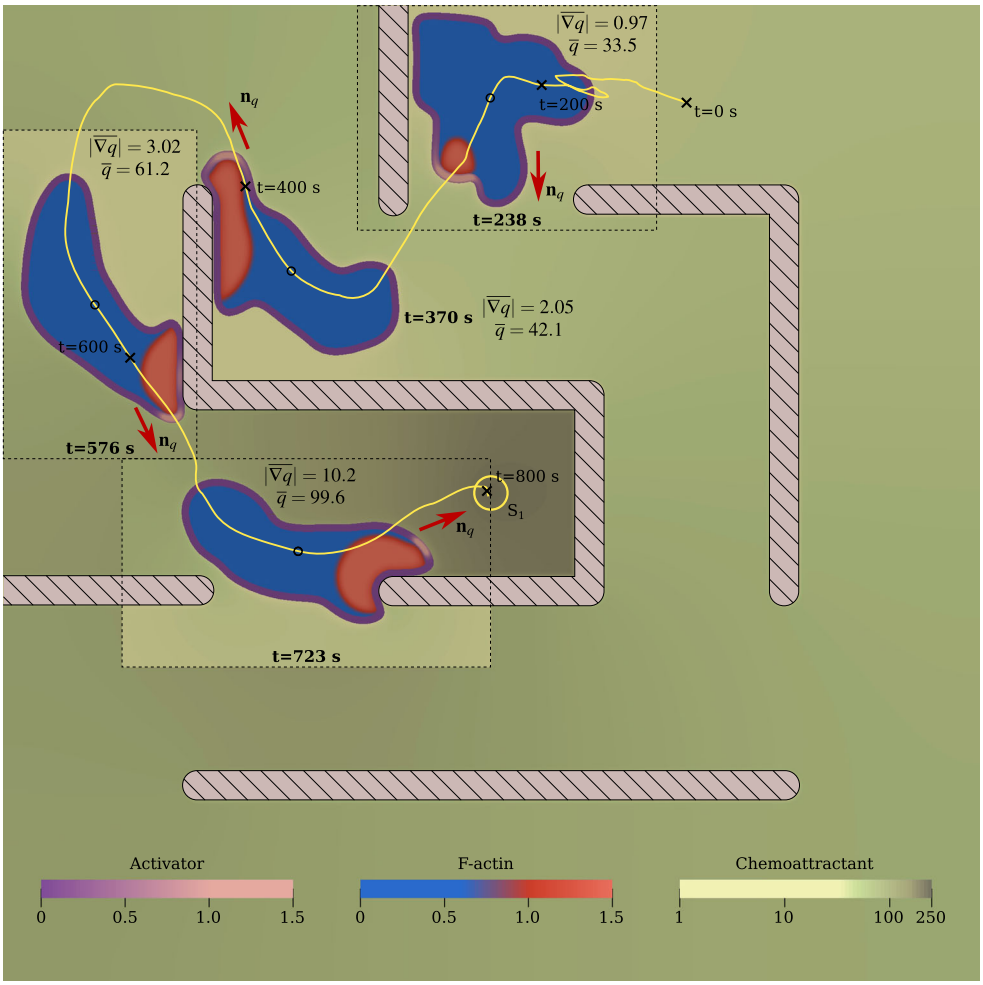

Fig. 9 Maze solving by chemotactic migration. Activator, F-actin, and chemoattractant distributions. We use the same mesh, initial cell geometry and time step as the simulation shown in Fig. 7. The cell is initially centered at the point (70, 90) µm. We set $D_q = 1000\ \mu\text{m}^2\text{s}^{-1}$ and $q_{\max,1} = 250$ nM. The chemotactic source S_1 (yellow circle) is active throughout the entire simulation. The walls are represented as striped grey regions (the width of the walls has been slightly modified for visualization purposes). The main panel shows the distributions of a, ρ_f, and q at $t = 370$ s. The three insets show the distributions of a, ρ_f, and q in the neighborhood of the cell at $t = 238$, 576, and 723 s. The cell's path is drawn with a yellow line. Black crosses represent the position of the mass center of the cell at $t = 0$, 200, 400, 600, and 800 s. $\mathbf{n}_q$ (red arrow), $|\overline{\nabla q}|$ and $\overline{q}$ (units nM/µm and nM, respectively) are indicated for the considered times $t = 238$, 370, 576, and 723 s. The position of the cell's center of mass is marked with a small circle

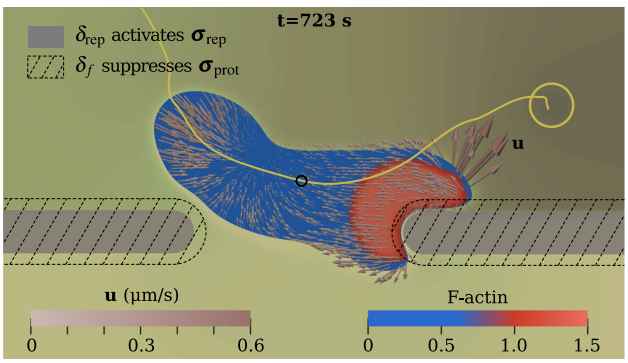

Fig. 10 Maze solving by chemotactic migration. F-actin distribution and F-actin network velocity (grey arrows) at $t = 723$ s. Protrusive stresses vanish in the striped regions. Repulsive stresses acting on the cell's membrane are activated in the grey regions

4.5 Three-dimensional migration on a planar substrate

In Sect. 4.3 we simulated migration on a planar substrate using a 2D computational model. While using a 2D simulation for this problem is common practice and produces indeed a reasonably accurate solution (see Ziebert and Aranson 2016), we show here that a 3D simulation allows to gain further insight into the process. In particular, the 2D approach somehow assumes that the entire surface of the cell is in contact with the substrate. However, experiments with *Dictyostelium* show that the cell displays irregular elongated shapes (Wessels et al. 2004), that produce only a few localized areas of contact with the substrate. The most common situation is that of two contact areas, where most of the adhe-

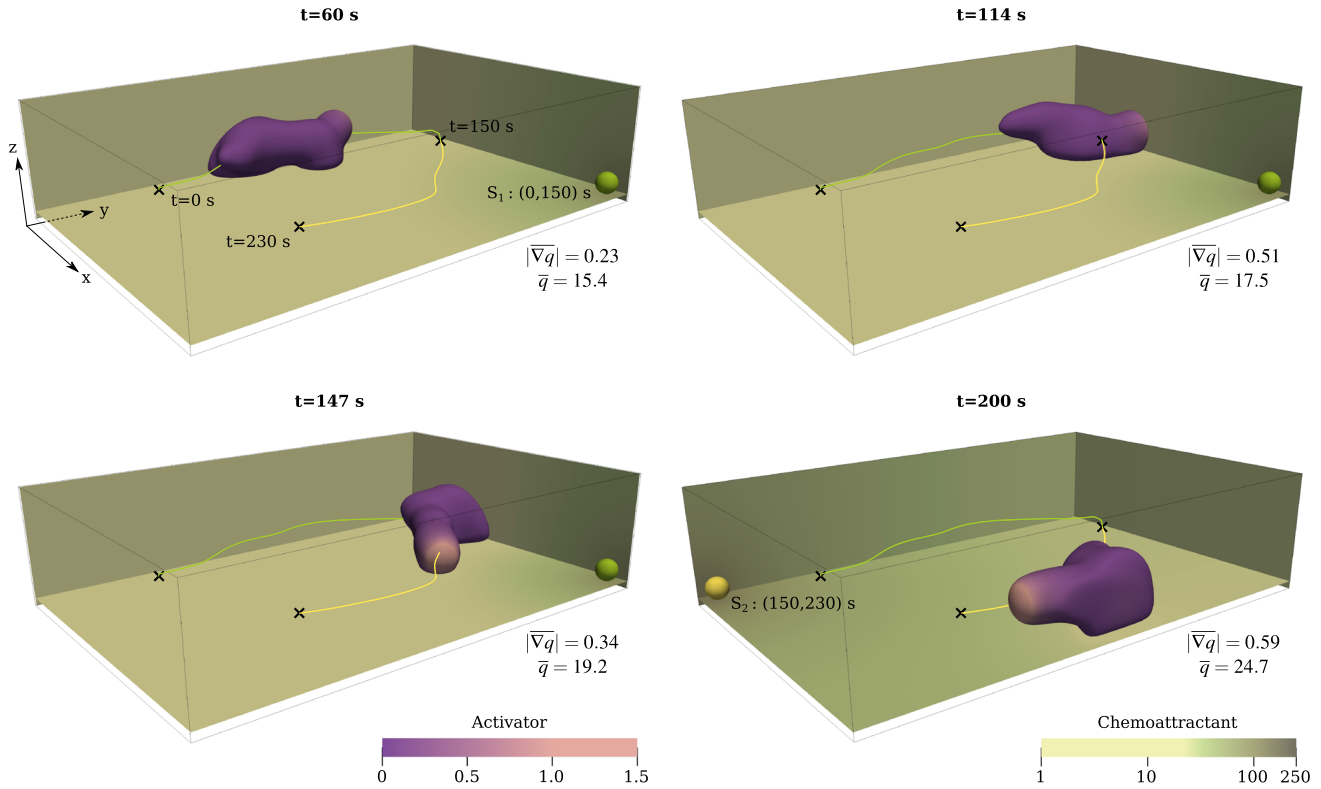

Fig. 11 3D migration on a planar substrate. Simulation performed on the box $[0, L_x] \times [0, L_y] \times [0, L_z]$ with $L_x = 43.2$, $L_y = 64.8$, and $L_z = 15.6\,\mu$m. The mesh is composed of $144 \times 216 \times 52$ $\mathscr{C}^1$-continuous quadratic elements. The initial time step is $\Delta t = 0.1$ s. The initial cell geometry is a cylinder of radius $R_c = 8\,\mu$m and height $h_c = 7\,\mu$m centered at the point $(12, 12, 4.5)\,\mu$m. We set $D_q = 400\,\mu\text{m}^2\text{s}^{-1}$, $q_{\max,1} = 150$ nM, and $q_{\max,2} = 250$ nM. The activator concentration is plotted on the cell membrane and the chemoattractant distribution on the planes $x = 0$, $y = L_y$, and $z = 1\,\mu$m, at $t = 60$, 114, 147, and 200 s. We also show the chemoattractant sources S_1 (green sphere) and S_2 (yellow sphere). The cell's path is divided into two segments according to the active source (S_1 green line, S_2 yellow line). The two sections are delimited with crosses

sive forces are located. The contact regions are at the front and the back of the cell with forces pointing in opposite directions and producing the so-called dipole of forces (del Álamo et al. 2007). Cell motion is a consequence of forces pointing forward being greater than forces pointing backwards. To better understand this process, we use our 3D computational model considering punctual adhesive forces on the substrate. Our computational domain is the box shown in Fig. 11. Since the cell location is defined using a diffuse interface representation, where the cell membrane has a thickness of order $\sim\varepsilon$, we consider the substrate to be the plane $z = \varepsilon/2 = 1\,\mu$m. The remaining boundaries of the domain (lateral and top) are non-adhesive walls where contact forces are not considered. To mimic a quasi-2D motion, we only allow the formation of new pseudopods in the region $z \in (z_{\text{cell}} - 1, z_{\text{cell}} + 1)\,\mu$m, where z_{cell} is the z-coordinate of the cell's center of mass. The chemotactic source S_q is defined as $S_q = S_1 + S_2$, where S_1 and S_2 have the usual spatial distribution and are centered at the points $\mathbf{S}_1^c = (41.2, 62.8, 2.5)$, $\mathbf{S}_2^c = (2, 2, 2.5)\,\mu$m. S_1 and S_2 are active, respectively, in the time intervals (0, 150) and (150, 230) s. Figure 11 shows the activator distribution on the cell's membrane and the chemoattractant concentration on the substrate as well as on two lateral boundaries. The plot also shows the path followed by the cell's center of mass throughout the simulation and the location of the active chemoattractant source at each time. The line representing the cell's path is divided in two sections, corresponding to the time intervals of activity of the chemoattractant sources. In the simulation, the signaling parameters $|\overline{\nabla q}|$ and $\overline{q}$ attain values ($|\overline{\nabla q}| \sim 0.5$ nM/μm and $\overline{q} \sim 20$ nM) that effectively bias the cell movement as illustrated by the cell's path. Figure 12 shows myosin concentration on the cell's membrane at the same times. As expected, myosin concentration is higher at the back of the cell. Figure 12 shows also insets with the punctual adhesive forces acting on the F-actin network[8]. The insets display the regions where the cell touches the substrate (black solid line) and the adhesive forces acting on them. The punctual forces are predominantly horizontal, effectively

[8] There are forces of equal strength and opposite direction acting on the substrate but we do not plot them for clarity.

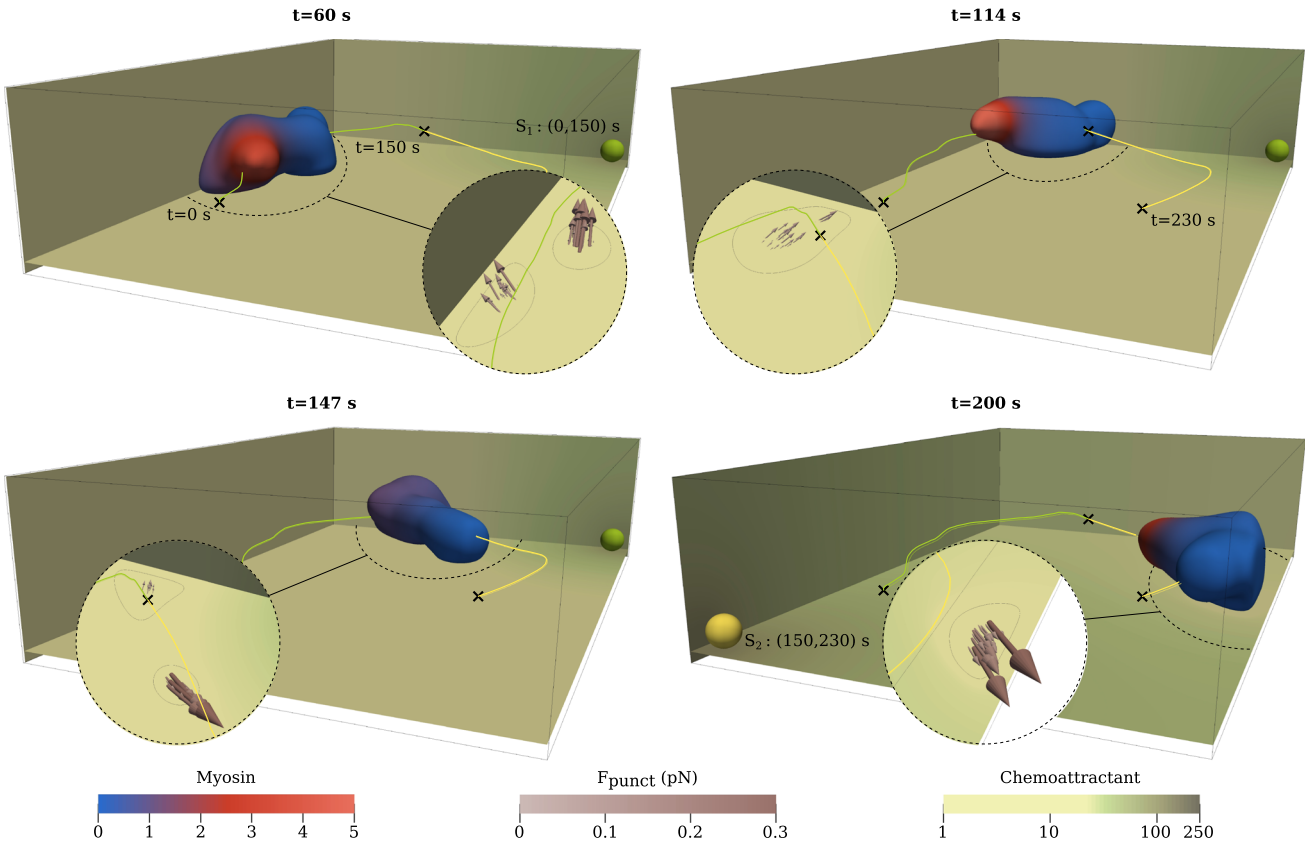

Fig. 12 3D migration on a planar substrate. Myosin distribution on the cell membrane and chemoattractant concentration on the planes $x = 0$, $y = L_y$, and $z = 1$ μm. The circular insets show the punctual adhesive forces $\mathbf{F}^j_{\text{punct}}$ (grey arrows) and the region of cell-substrate contact (black solid line)

contributing to the cell's motion. At times $t = 60$ s and $t = 147$ s the dipole of forces seen experimentally emerges naturally in the simulations, although the imbalance of forces seems to be greater than in experiments (del Álamo et al. 2007). In particular, the contractile pole exerts much smaller forces than the protrusive pole; see $t = 147$ s. At some points ($t = 114$ s and $t = 200$ s), the cell's tail even detaches from the substrate and there is no contractile pole. These observations indicate that future modeling efforts should be directed at improving our description of punctual adhesions. We also believe that this example can be an important benchmark as the field of computational cell migration transitions from 2D to 3D simulations.

4.6 Three-dimensional migration in a fibrous environment

Our previous examples focus on cell motion on a planar substrate, but most cells actually migrate within the extracellular matrix interacting chemically and mechanically with a fibrous network. While migrating through the extracellular matrix, cells establish adhesions and remodel the fibers by deforming and degrading them. Our current model cannot handle all of these phenomena, but we aim at reproducing a much simpler scenario in which the fibers are rigid and the cell is unable to degrade them. In our simplified computation, the fibers are represented by cylindrical objects where the cells can establish punctual adhesions. The layout of the fibers can be observed in Fig. 13, where the width of the fibers has been slightly reduced for a better visualization of the cell. The computation was performed on a cubic domain. The boundaries of the cube are assumed to be non-adherent walls, where the cell cannot establish punctual adhesions. The cell's migration is driven by the chemotactic source $S_q = S_1 + S_2$, where the S_i's have the usual form. The sources are centered at $\mathbf{S}^c_1 = (36, 36, 36)$ and $\mathbf{S}^c_2 = (2, 2, 2)$ μm. The chemoattractant sources S_1 and S_2 are active in the time intervals $(0, 140)$ and $(140, 350)$ s, respectively. Figure 13 shows the activator distribution on the cell's membrane. The plot also displays the location of the active chemoattractant source with a small sphere. Three faces of the cube have been colored according to the chemoattractant concentration. Figure 14 follows the same format, but shows the myosin concentration on the cell's membrane using a reduced view from a different perspective. From the figures, we can see that the values of the signaling parameters ($|\overline{\nabla q}| \sim 0.2$ nM/μm and

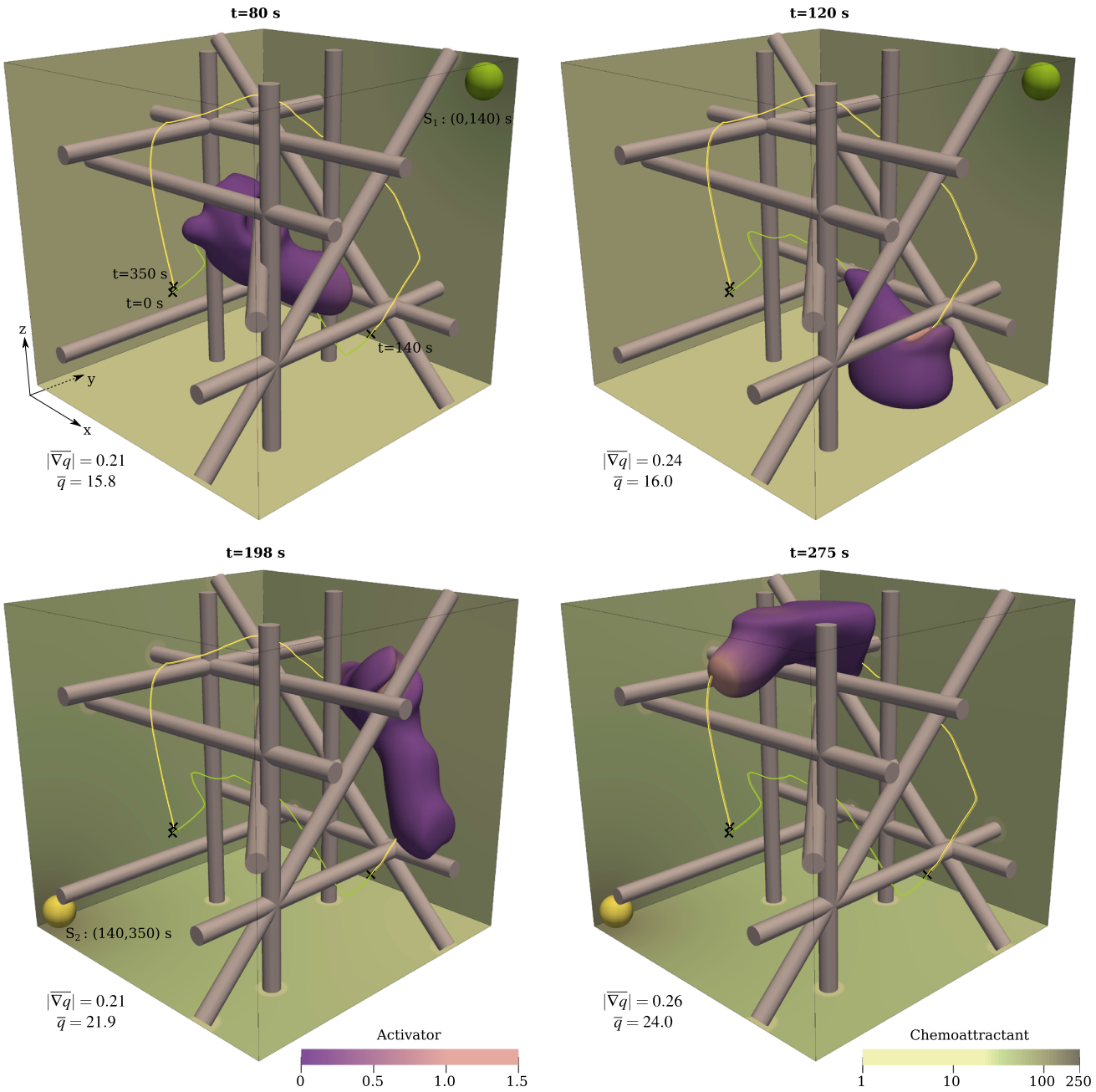

Fig. 13 3D migration in a fibrous environment. The simulation is performed on the cube $[0, L]^3$ with $L = 38.4\,\mu$m. The mesh is comprised of 128 $\mathscr{C}^1$-continuous quadratic elements in each direction. The initial time step is $\Delta t = 0.1$ s and the initial cell geometry is a sphere of radius $R_c = 7\,\mu$m centered at the point $(12, 12, 12)\,\mu$m. We set $D_q = 400\,\mu\text{m}^2\text{s}^{-1}$, $q_{\max,1} = 150$ nM, and $q_{\max,2} = 250$ nM. The activator density is plotted on the cell membrane and the chemoattractant distribution on three walls of the domain, at $t = 80$, 120, 198, and 275 s. We also plot the chemotactic sources S_1 (green sphere) and S_2 (yellow sphere). The fibers' width has been slightly reduced for visualization purposes. The cell's path is divided into two sections corresponding to the different active sources (green line for S_1, yellow line for S_2). The crosses on the cell's path mark the position of the cell's center of mass at $t = 0$, 140, and 350 s

$\overline{q} \sim 20$ nM) fall within a range where significant chemotactic bias is expected. Thus, despite the presence of the fibers that impede a more straight migration, the cell gradually approaches the active chemoattractant source as illustrated by the path traveled by the cell's center of mass. Throughout the simulation, the cell touches the fibers and the boundary. The cell–fiber interaction modifies the motion of the cell, as well as the cell shape (see, e.g., $t = 80$ s where a fiber is surrounded by the cell's body). In addition, the interaction with fibers gives rise to punctual adhesions, which produce

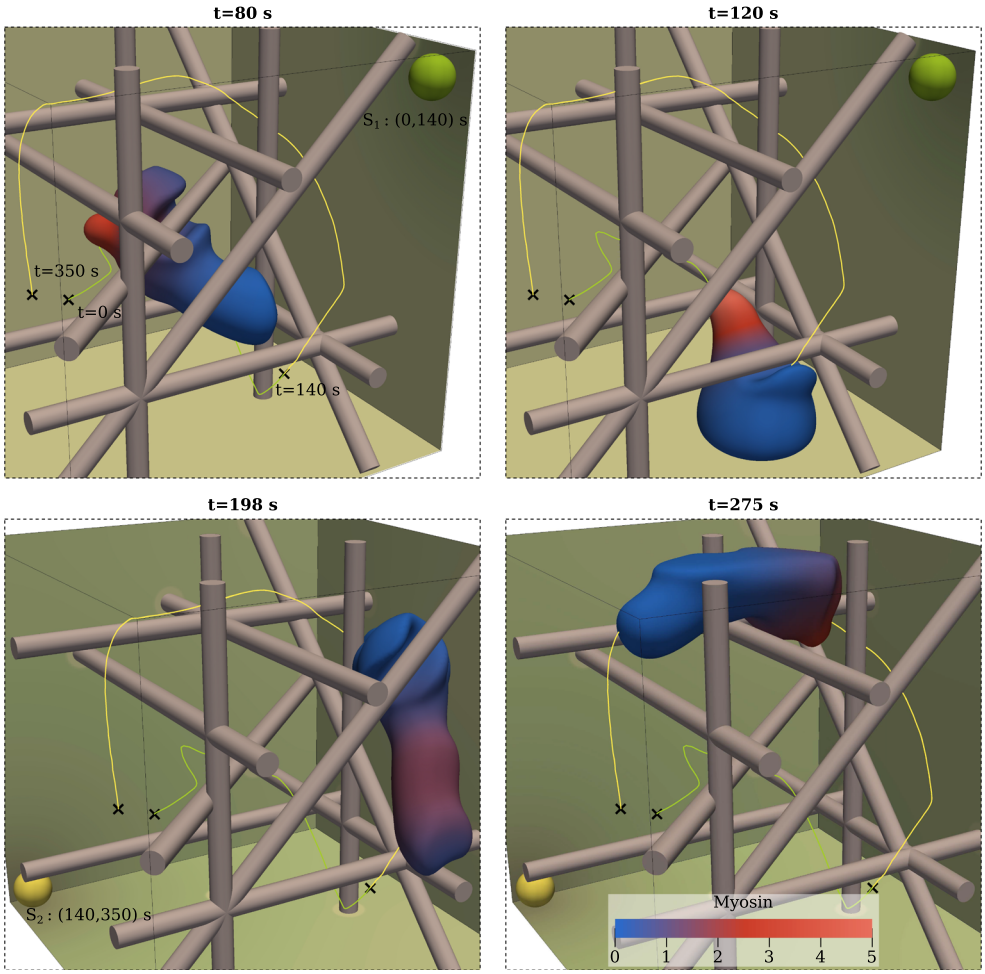

Fig. 14 3D migration in a fibrous environment. The myosin distribution is plotted on the cell membrane and the chemoattractant concentration on three walls of the domain

an increase of the cell–fiber adhesiveness (see, e.g., $t = 198$ s where the tail of the cell remains attached to the fibers producing a noticeable deformation of the cell's body).

4.7 Model limitations

4.7.1 Signaling mechanisms of chemotaxis

We have simplified the reactions of the signaling compounds by considering a single activator. In our model, the activator dynamics is controlled by statistical data (see Fig. 3) that are biased according to extracellular signals. Thus, the activator displays a phenomenological behavior based on statistics taken from 2D experiments. Such data does not seem to be available in 3D. Therefore, we proposed an extension to 3D of the functions shown in Fig. 3a, but this remains to be validated.

Cellular chemotaxis features signal amplification and adaptation: Small variations ($\sim 2\%$) in the chemoattractant concentration over the cell's length produce chemotaxis due to the amplification of the external signal (Janetopoulos et al. 2004). Although the exact mechanisms that control signal amplification are not understood, our model is able to replicate amplification through the signaling parameters, as shown in the simulations. However, as seen in Sect. 4.2, the model is unable to reproduce adaptation, i.e., the change of the chemotactic response as a function of the time evolution of the chemoattractant concentration. Adaptation not only explains *Dictyostelium* aggregation, but also the cell's behavior after the exposure to a uniform chemoattractant concentration (Van Haastert and Devreotes 2004): A moving cell exposed to a sudden increase in the chemoattractant concentration undergoes actin polymerization along the entire membrane for a short period of time (~ 6 s). Due to the polymerization of the entire membrane, the cell stops its motion and remains still for some time. After that, even if the chemoattractant concentration remains constant, a gradual actin depolymerization takes place, permitting the cell to return to its original polarized and motile state. Adaptation could be incorporated to our model by considering a

more accurate description of the dynamics of the membrane-signaling compounds; see, e.g., Levchenko and Iglesias (2002) or Ribeiro et al. (2017).

4.7.2 Punctual adhesions

The adhesion between the cell and the extracellular environment is a complex process carried out by a family of transmembrane proteins called integrins. Cells express different levels of adhesion depending on the mode of migration they are performing (Friedl and Wolf 2009). Amoeboid cells exhibit weak adhesions to the environment. In fact, some amoeboid cells can migrate in the absence of integrin (Lämmermann et al. 2008). In contrast, mesenchymal cells develop strong adhesions, where integrins cluster and form the so-called focal adhesions. Focal adhesion formation involves a series of steps (initiation, integrin clustering, growth, and maturation) highly regulated by actomyosin contractility and extra- and intra-cellular signals (Geiger et al. 2009). In this paper, we have simplified punctual adhesions as gripping forces whose spring constants increase with time. In our model, punctual adhesions disassemble following Bell's law (see "Appendix A2"). The parameter F_0 controls the strength of the punctual adhesion. Thus, F_0 can be adjusted to represent either weak or strong (focal) adhesions. To improve the model, myosin contractility and F-actin network dynamics should be taken into account in the process of maturation and rupture. In addition, focal adhesions usually change the mechanism of force transmission between a gripping and a slipping mode (Jurado et al. 2005); and we have only considered gripping forces in the model.

Finally, rigid fibers do not reproduce the features of the extracellular matrix where actual cells migrate. Taking into account the elasticity of the fibers, as well as considering extracellular matrix degradation, may lead to more realistic results.

5 Conclusions

We propose a phase-field model for chemotactic motion of amoeboid cells. The model, which attains cell motion by considering the forces acting on the actomyosin network, captures the reactions occurring along the signaling pathway. The underlying computational technology is the diffuse domain method, which permits to solve equations posed on deformable domains (i.e., the cytosol, the membrane, and the extracellular medium) using a fixed mesh only. The results show quantitative agreement with experiments, though some experimentally observed features of chemotactic motion are not observed due to the stochastic description used for pseudopod formation. In addition, including the cell-substrate (or cell–fiber) interaction leads to realistic 3D migration on substrates (or in fibrous networks). The results also suggest that coupling the extracellular, membrane, and cytosol dynamics is crucial to better understand chemotaxis, especially in case of migration in confined environments. The model may be improved by including a deterministic theory for the membrane signaling molecules reactions. In addition, considering fiber elasticity and matrix degradation, along with the focal adhesions may provide new insights and extend the model to other directional migrations, such as haptotaxis or durotaxis.

Acknowledgements A.M. and H.G. were partially supported by the European Research Council (Contract # 307201) and by Consellería de Cultura, Educación e Ordenación Universitaria (Xunta de Galicia). A.M. was partially supported by the UDC-Inditex Ph.D. student grant program.

Compliance with ethical standards

Conflict of interest The authors declare that they have no conflict of interest.

Appendix

A1: Diffuse domain approach

The classic approach to solve the dynamics of a generic compound $\rho_c(\mathbf{x}, t)$ inside the cell is to pose the governing equation on a moving domain $\Omega_c(t)$, where $\Omega_c(t)$ denotes the spatial region occupied by the cell. Let us consider the convection–diffusion–reaction problem

$$\frac{\partial \rho_c}{\partial t} + \nabla \cdot (\rho_c \mathbf{u}_c) = \nabla \cdot (D_c \nabla \rho_c) + r_c \rho_c \quad \text{in } \Omega_c(t), \tag{14}$$

$$D_c \nabla \rho_c \cdot \mathbf{n} + \rho_c (\mathbf{u}_\Gamma \cdot \mathbf{n} - \mathbf{u}_c \cdot \mathbf{n}) = -j \quad \text{on } \Gamma_c(t), \tag{15}$$

where D_c and r_c are the diffusion and reactive coefficients, respectively, and $\mathbf{u}_c$ is the bulk velocity of ρ_c. We define the cell membrane as $\Gamma_c(t) = \partial \Omega_c(t)$. We call $\mathbf{n}$ the unit outward normal to $\Gamma_c(t)$ and $\mathbf{u}_\Gamma$ the velocity of $\Gamma_c(t)$. Note that, $\mathbf{u}_c$ and $\mathbf{u}_\Gamma$ do not necessarily have to coincide. The boundary condition in Eq. (15) equates the convective–diffusive flux across the membrane to the prescribed value j.

Let us also consider a compound $\rho_\Gamma(\mathbf{x}, t)$ living in the membrane $\Gamma_c(t)$. The surface PDE that governs the dynamics of ρ_Γ is

$$\frac{\partial \rho_\Gamma}{\partial t} + \nabla_\Gamma \cdot (\rho_\Gamma \mathbf{u}_\Gamma) = \nabla_\Gamma \cdot (D_\Gamma \nabla_\Gamma \rho_\Gamma) + r_\Gamma \rho_\Gamma + j \quad \text{in } \Gamma_c(t), \tag{16}$$

where ∇_Γ denotes the operator ∇ on the surface Γ_c. D_Γ and r_Γ are the diffusion and reactive parameters, respectively. Note that, the unknowns ρ_c and ρ_Γ are coupled through

the mass flux term j. Eqs. (14)–(16) define the so-called sharp-interface problem. The numerical solution of the sharp-interface problem requires the use of volumetric and surface moving meshes and an algorithm to transfer information between the two meshes.

The diffuse domain approach allows a simpler treatment of the former problem. We consider a larger and fixed domain Ω such that $\Omega_c(t) \subset \Omega$ and we resort to the spatial markers ϕ and δ_m that locate the cell and the membrane, respectively; see Sect. 2.1 in the main text. We assume now that ρ_c and ρ_Γ are defined on Ω. Assuming (momentarily) that ρ_Γ is extended off Γ_c constant in the normal direction,[9] i.e., $\nabla\rho_\Gamma \cdot \mathbf{n} = 0$, we can state the equivalent diffuse-interface problem as

$$\frac{\partial(\phi\rho_c)}{\partial t} + \nabla\cdot(\phi\rho_c\mathbf{u}_c) = \nabla\cdot(\phi D_c\nabla\rho_c) + \phi r_c\rho_c - \delta_m j \quad \text{in } \Omega, \tag{17}$$

$$\frac{\partial(\delta_m\rho_\Gamma)}{\partial t} + \nabla\cdot(\delta_m\rho_\Gamma\mathbf{u}_\Gamma) = \nabla\cdot(\delta_m D_\Gamma\nabla\rho_\Gamma) + \delta_m r_\Gamma\rho_\Gamma + \delta_m j \quad \text{in } \Omega. \tag{18}$$

It has been proven (Li et al. 2009; Teigen et al. 2009) that Eqs. (17)–(18) converge to Eqs. (14)–(16) as the regularization parameter (ε in our model) tends to 0. The governing laws for cytosol dynamics in our model [Eqs. (4), (7), and (8)] are based on Eq. (17), while the activator equation is based on Eq. (18). We took $j = 0$, which indicates that we do not consider directly the reactions of the activator with intracellular elements. That interaction is accounted for through the functional $\mathscr{F}$ in Eq. (5) and the signaling parameters $\overline{\nabla q}$ and $\overline{q}$. In addition, the membrane displacement is driven by the F-actin network velocity, such that $\mathbf{u}_\Gamma = \mathbf{u}$ in the activator equation. The equation that governs chemoattractant dynamics is based on Eq. (17), but the function ψ plays the role of ϕ as a spatial marker.[10] Additionally, for the chemoattractant, we do not consider extracellular advection, that is, $\mathbf{u}_c = 0$. The ligand-receptor binding is modeled taking $j = k_q q$.

A2: Model details

Obstacle localizers

In Eq. (11), the term δ_f annihilates protrusive stresses in the vicinity of the obstacles, while δ_{rep} activates repulsive forces when the cell approaches an obstacle. In this work, excluding the examples computed using periodic boundary conditions, we assume that the unknown ϕ vanishes on the boundary. In that case, the boundary behaves as a rigid obstacle that impedes the movement of the cell. To define δ_f and δ_{rep} we resort to the fields $d_o(\mathbf{x})$ and $d_b(\mathbf{x})$. The field $d_o(\mathbf{x})$ provides the distance to obstacles that we place on the domain and $d_b(\mathbf{x})$ accounts for the distance between point $\mathbf{x}$ and the closest non-periodic boundary. The marker δ_f is expressed as

$$\delta_f = \begin{cases} \mathscr{H}(d_o(\mathbf{x}) - d_o^f) & \text{if } \ d_o(\mathbf{x}) < d_b(\mathbf{x}) + \Delta d^f \\ \mathscr{H}(d_b(\mathbf{x}) - d_b^f) & \text{if } \ d_o(\mathbf{x}) \geq d_b(\mathbf{x}) + \Delta d^f, \end{cases} \tag{19}$$

where $\Delta d^f = d_o^f - d_b^f$, with $d_o^f = 2.6\ \mu\text{m}$ and $d_b^f = 1.8\ \mu\text{m}$. Both d_o^f and d_b^f are effective distances at which the cell starts to suppress protrusive stress when approaching an obstacle and the boundary, respectively. Note that if we consider periodic boundary conditions, $d_b(\mathbf{x}) \to \infty$ and $\delta_f = \mathscr{H}(d_o(\mathbf{x}) - d_o^f)$. We define $\delta_{\text{rep}} = \mathscr{H}(d_o^{\text{ef}} - d_o(\mathbf{x}))$, which does not depend on $d_b(\mathbf{x})$. Thus, the repulsive force is not active on the boundary because the boundary condition $\phi = 0$ produces the same effect as $\boldsymbol{\sigma}_{\text{rep}}$. However, if δ_f does not suppress the protrusive force on the boundary, an instability in the balance of forces appears and the cell undergoes a backward movement not observed in experiments.

Punctual adhesive forces

Punctual adhesions are modeled as springs. We call N_{adh} the number of adhesions active at a particular time. We assume that N_{adh} cannot exceed the value $N_{\text{adh}}^{\max}$. Each punctual adhesion is associated to an index j such that $1 \leq j \leq N_{\text{adh}}$. We suppose that the spring associated to the adhesion j has one end fixed at the substrate at point $\mathbf{x}_0^j$ and the other end attached to the F-actin network at point $\mathbf{x}^j$. The spring j produces a force per unit volume $\mathbf{F}_{\text{punct}}^j = -k_{\text{grip}_0}(t - t_0^j)(\mathbf{x}^j - \mathbf{x}_0^j)\delta(\mathbf{x} - \mathbf{x}^j)$, where $\mathbf{x}^j$ moves according to the velocity $\mathbf{u}$, t_0^j is the time at which adhesion j is formed, and k_{grip_0} is a constant. The initial deformation of the spring is zero, that is $\mathbf{x}_0^j = \mathbf{x}^j(t_0^j)$. When we advance from t_n to $t_{n+1} = t_n + \Delta t$ in our time-stepping scheme, we update the punctual adhesion states as follows:

1 Determine the position of the N_{adh} points $\mathbf{x}^j$ at time t_{n+1}:

$$\mathbf{x}^j(t_{n+1}) = \mathbf{x}^j(t_n) + \int_{t_n}^{t_{n+1}} \mathbf{u}(\mathbf{x}^j(\tau), \tau)\mathrm{d}\tau. \tag{20}$$

Eq. (20) may be replaced by the approximation $\mathbf{x}^j(t_{n+1}) = \mathbf{x}^j(t_n) + \mathbf{u}(\mathbf{x}^j, t_n + \Delta t/2)\Delta t$.

2 Determine which punctual adhesions will break during the current time step. The rupture of punctual adhe-

[9] It can be shown using Eq. (18) that, to leading order, this assumption holds true.

[10] Although we have referred to Ω_c as the cell, the rationale applies also to the extracellular environment which is internally bounded by Γ_c. When we use Eq. (17) for the chemoattractant, Ω_c does, indeed, represent the extracellular space.

sions follows a stochastic model based on Poisson's distribution[11] with average number of events per interval $\lambda_p^j = r_{\text{off}}^j(t_{n+1} - t_0^j)$, where j is the index that identifies the punctual adhesion. The dissociation rate $r_{\text{off}}^j = r_{\text{off}_0} \exp(|\mathbf{F}_{\text{punct}}^j|/F_0)$ is modeled using Bell's law (Bell 1978), where r_{off_0} is a constant and F_0 the characteristic adhesive strength. We also consider that if the point $\mathbf{x}^j$ leaves the cell ($\phi(\mathbf{x}^j) < 1/4$), then the adhesion j is broken.

3 Remove broken adhesions and update N_{adh}.

4 If $N_{\text{adh}} < N_{\text{adh}}^{\max}$, find new points $\mathbf{x}^j$ such that:

- $\phi(\mathbf{x}^j) \sim 1/2$.
- $d_o(\mathbf{x}^j) \lesssim d_o^{\text{ef}}$ or $d_b(\mathbf{x}^j) \lesssim \varepsilon/2$ ($\mathbf{x}^j$ falls in the substrate or fiber).
- $\mathbf{x}^j$ is sufficiently far away from existing adhesions. In particular, we only permit new punctual adhesions on elements of the computational mesh where no active adhesions are located. In addition, we only permit one new punctual adhesion per element.

If the set of points that verify these conditions provides more points than required to reach $N_{\text{adh}}^{\max}$, we choose a subset using a random distribution weighted by the F-actin density, so that those points with a higher F-actin density are more likely to become new adhesions. Otherwise, all points in the set become active adhesions.

5 Update N_{adh}.

Pseudopod formation

The activator equation [see Eq. (13)] resorts to the source term S_a to define peaks of activator that detonate the growth of new pseudopods. Each peak i appears for a certain period of time given by $\delta_{t,i}^a = \mathscr{H}(\Delta T_i - (t - \tau_{0,i}))$ for $t > \tau_{0,i}$, where ΔT_i is the growth time, defined in Sect. 2.4. $\tau_{0,i}$ is the time at which a new peak emerges. It is defined through the interval time $\Delta\tau_i$ such that $\tau_{0,i} = \tau_{0,i-1} + \Delta\tau_i$, with the initial peak arising at time $\tau_{0,1} = 0$. The spatial location of the peak i is given by $\delta_{\mathbf{x},i}^a = \mathscr{H}(R_a - d_i^a(\mathbf{x}))$, where $d_i^a(\mathbf{x})$ is the distance to the point $\mathbf{s}_i$, the center of the peak, and R_a is its approximate radius. In our model, based on the pseudopod-centered view, we first locate the point $\mathbf{s}_i^*$, which is the center of the activator peak without considering chemotaxis, and then we apply the chemotactic bias to get $\mathbf{s}_i$. The process to obtain $\mathbf{s}_i^*$ is illustrated in Fig. 3a for the 2D case. We divide the membrane starting from the location of $\mathbf{s}_{i-1}$ into two regions of equal length, such that we get $d_{i-1,\max}$ (see Fig. 3a, right). The probability of $\mathbf{s}_i^*$ being located on the same side of the membrane than $\mathbf{s}_{i-2}$ is $P_{\text{PE}}\beta_{\text{R/L}}/(1+\beta_{\text{R/L}})$. The probability of the opposite side of the membrane hosting $\mathbf{s}_i^*$ is $P_{\text{PE}}/(1+\beta_{\text{R/L}})$. The fact that the probabilities are different produces persistence: a higher tendency to alternate right–left extensions than to *hop* (consecutive left–left or right–right splitting).

The procedure to get $\mathbf{s}_i^*$ in the 3D case is slightly different. Let us consider a theoretical case where the cell shape is an ellipsoid with $\mathbf{s}_{i-1}$ and $\mathbf{s}_{i-2}$ placed in a mean equatorial plane (see Fig. 3c, left). The plane π_1, which contains $\mathbf{s}_{i-1}$, $\mathbf{s}_{i-2}$, and $\mathbf{x}_{\text{cell}}$ (the mass center of the cell), presents a probability distribution analogous to that of the 2D case. However, the plane π_2, which is orthogonal to π_1 (in particular, orthogonal to the line that joins $\mathbf{s}_{i-1}$ and $\mathbf{x}_{\text{cell}}$), shows that the probability of extension decreases proportional to the distance to the plane π_1. Thus, the probability of extension is zero on a large region of the cell surface (see Fig. 3c, middle). Nevertheless, an actual cell exhibits more complicated shapes. We approximate the theoretical probability distributions as follows: From point $\mathbf{s}_{i-1}$, we compute the geodesic distance over the cell surface to get $d_{i-1,\max}$. We resort to the probability function P_{PE} (see Fig. 3a, middle) to obtain d_{i-1} and the corresponding value of $\beta_{\text{R/L}}$. $\mathbf{s}_i^*$ will be located in l_d, defined as the set of points of the membrane whose distance from $\mathbf{s}_{i-1}$ is d_{i-1} . We select the points C_{l_d} and D_{l_d}, which are the closest and farthest points to $\mathbf{s}_{i-2}$ belonging to l_d, respectively. The probability of extension along l_d presents two triangles centered on C_{l_d} and D_{l_d}. The length of the base of each triangle is 10% of the total length of l_d, and the probability at points C_{l_d} and D_{l_d} is $\beta_{\text{R/L}}/(1+\beta_{\text{R/L}})$ and $1/(1+\beta_{\text{R/L}})$, respectively. The similarity with the theoretical case may be noted if we assume that the view in π_2 (Fig. 3c, middle) corresponds to l_d. The point $\mathbf{s}_i$ is obtained from $\mathbf{s}_i^*$ through to the process explained in the main text (Sect. 2.4) and "Appendix A3". In the 3D case, we follow the same rationale to get $\mathbf{s}_i$, so that $\mathbf{n}_q$, $\mathbf{n}_{\mathbf{s}_i^*}$, and $\mathbf{n}_{\mathbf{s}_i}$ belong to the same plane; see Fig. 3c (right). In the case of cell-obstacle contact, we prevent pseudopod extension by modifying the probability distribution P_{PE} such that $P_{\text{PE}}(\mathbf{x}) = 0$ if $d_o(\mathbf{x}) < 2.35\,\mu\text{m}$ or $d_b(\mathbf{x}) < 1.55\,\mu\text{m}$.

A3: Additional implementation details

Weak form of the model

The weak form can be written as:

$$\int_\Omega w_1 \frac{\partial\phi}{\partial t}\mathrm{d}\Omega + \int_\Omega w_1\,\mathbf{u}\cdot\nabla\phi\mathrm{d}\Omega + \int_\Omega \Gamma_\phi\varepsilon\nabla w_1\cdot\nabla\phi\mathrm{d}\Omega + \int_\Omega w_1\Gamma_\phi\frac{G'}{\varepsilon}\mathrm{d}\Omega - \int_\Omega \Gamma_\phi\varepsilon\nabla w_1\cdot\nabla\phi\mathrm{d}\Omega - \int_\Omega w_1\frac{\Gamma_\phi\varepsilon}{|\nabla\phi|}\nabla\phi\cdot\nabla(|\nabla\phi|)\mathrm{d}\Omega = 0, \tag{21}$$

[11] The Poisson distribution states that the probability of observing k events in an interval is given by the equation $P = \exp(-\lambda_p)\lambda_p^k/k!$, where λ_p is the average number of events per interval. In our adhesion rupture model, $k = 1$ and $\lambda_p^j = r_{\text{off}}^j(t - t_0^j)$, where the index j identifies the punctual adhesion.

$$\int_\Omega w_2 \frac{\partial(\phi\rho_m)}{\partial t}\mathrm{d}\Omega - \int_\Omega \nabla w_2 \cdot \mathbf{u}\phi\rho_m \mathrm{d}\Omega + \int_\Omega D_m \phi \nabla w_2 \cdot \nabla \rho_m \mathrm{d}\Omega = 0, \tag{22}$$

$$\int_\Omega w_3 \frac{\partial(\phi\rho_f)}{\partial t}\mathrm{d}\Omega - \int_\Omega \nabla w_3 \cdot \mathbf{u}\phi\rho_f \mathrm{d}\Omega + \int_\Omega \varepsilon_f^2 \phi \nabla w_3 \cdot \nabla \rho_f \mathrm{d}\Omega + \int_\Omega w_3 \phi \frac{\partial F}{\partial \rho_f}\mathrm{d}\Omega - \int_\Omega w_3 \lambda_N \phi \mathrm{d}\Omega = 0, \tag{23}$$

$$- \int_\Omega \nabla \mathbf{w}_4\, \phi[\mu(\nabla\mathbf{u} + \nabla\mathbf{u}^T) + \lambda(\nabla\cdot\mathbf{u})\mathbf{I}]\mathrm{d}\Omega - \int_\Omega \nabla \mathbf{w}_4\, \phi\rho_m\eta_m\mathbf{I}\mathrm{d}\Omega + \int_\Omega \nabla \mathbf{w}_4\, \phi\rho_f\eta_f\delta_f\nabla\phi\otimes\nabla\phi\mathrm{d}\Omega - \int_\Omega \varsigma \mathbf{w}_4 \cdot \mathbf{u}\mathrm{d}\Omega + \sum_j \mathbf{w}_4(\mathbf{x}^j)\cdot\mathbf{F}^j_{\text{punct}} - \int_\Omega \gamma\, \mathbf{w}_4 \cdot \nabla\phi(\varepsilon\nabla^2\phi - \frac{G'}{\varepsilon})\mathrm{d}\Omega - \int_\Omega \nabla \mathbf{w}_4\, \phi\eta_{\text{rep}}\delta_{\text{rep}}\nabla\phi\otimes\nabla\phi\mathrm{d}\Omega = 0, \tag{24}$$

$$\int_\Omega w_5 \frac{\partial(\psi q)}{\partial t}\mathrm{d}\Omega + \int_\Omega D_q\psi\nabla w_5\cdot\nabla q\mathrm{d}\Omega + \int_\Omega w_5 r_q \psi q \mathrm{d}\Omega - \int_\Omega w_5 b_q \psi S_q \mathrm{d}\Omega + \int_\Omega w_5 k_q \delta_m q \mathrm{d}\Omega = 0, \tag{25}$$

$$\int_\Omega w_6 \frac{\partial(\delta_m a)}{\partial t}\mathrm{d}\Omega - \int_\Omega \nabla w_6 \cdot \mathbf{u}\delta_m a\mathrm{d}\Omega + \int_\Omega D_a\delta_m\nabla w_6\cdot\nabla a\mathrm{d}\Omega + \int_\Omega w_6 r_a \delta_m a \mathrm{d}\Omega - \int_\Omega w_6 b_a \delta_m S_a \mathrm{d}\Omega = 0, \tag{26}$$

where $\{w_i(\mathbf{x})\}_{i=1,\ldots,6}$ are the weighting functions. Note that, some of the terms in the weak form become singular outside of the cell and they are computed using a similar procedure to that described in Moure and Gomez (2017). We obtain the Galerkin form by replacing in Eqs. (21)–(26) the unknowns and the weighting functions with discrete approximations. For example, we replace $\phi(\mathbf{x}, t)$ with

$$\phi^h(\mathbf{x}, t) = \sum_A \phi^A(t) N^A(\mathbf{x}), \tag{27}$$

where the N^A's are spline basis functions, and the ϕ^A's are referred to as control variables. Likewise, we replace the weighting functions $w_i(\mathbf{x})$ with $w_i^h(\mathbf{x}) = \sum_A w_i^A N^A(\mathbf{x})$.

Linear algebra

The linear system that needs to be solved in the Newton–Raphson algorithm is ill-conditioned because most of the unknowns approach zero in different regions of Ω (e.g., the chemoattractant concentration is almost zero inside the cell and the cytosolic components outside the cell). To improve the condition number without altering the solution, we replace the appropriate rows of the tangent matrix by the corresponding rows of the identity matrix, as well as the associated elements of the residual vector by 0; see Moure and Gomez (2017) for more details. The procedure explained for the cytosolic variables based on the value of ϕ, is extended in a similar way for q, based on the value of ψ. Here, we take the thresholds $\psi^T = \phi^T = |\nabla\phi|^T = 10^{-8}$.

Discrete compartment

The integration demanded by the numerical method is done through element-based Gaussian quadrature. The evaluation of any unknown on points other than Gauss points slows down the computations. Hence, instead of applying each punctual adhesive force $\mathbf{F}^j_{\text{punct}}$ at $\mathbf{x}^j$, we apply $\mathbf{F}^j_{\text{punct}}$ at the closest Gauss point to $\mathbf{x}^j$. Regarding the pseudopod formation description (see Sect. 2.4 and "Appendix A2"), $\mathbf{s}_i^*$ is placed at the closest Gauss point to its theoretical position. To obtain $\mathbf{s}_i$, we need to compute angles and normal vectors to the membrane. To speed up the computations, we only do that at Gauss points. We resort to penalty functions to select the Gauss point that best adjusts to the point $\mathbf{s}_i$ we seek. Let us call $G_M = \{\mathbf{x}_i^G\}_{i=1,\ldots,N_G}$ the set of Gauss points located at the cell's membrane and sufficiently far away from obstacles, that is, $\phi(\mathbf{x}_i^G) \approx 1/2$, $d_o(\mathbf{x}_i^G) \geq 2.35\ \mu\text{m}$, and $d_b(\mathbf{x}_i^G) \geq 1.55\ \mu\text{m}$. In 2D we replace $\mathbf{s}_i$ with the point of G_M that minimizes the penalty function $PF_{2\text{D}}(\mathbf{x}_i^G) = |\widehat{\mathbf{n}_q, \mathbf{n}_{\mathbf{x}_i^G}} - \omega_i| + 1.5 d_{\mathbf{s}_i^*}(\mathbf{x}_i^G)$, where $\widehat{\mathbf{n}_q, \mathbf{n}_{\mathbf{x}_i^G}}$ is the angle formed by $\mathbf{n}_q$ and $\mathbf{n}_{\mathbf{x}_i^G}$ in degrees, and $d_{\mathbf{s}_i^*}(\mathbf{x}_i^G)$ is the distance between $\mathbf{s}_i^*$ and $\mathbf{x}_i^G$ in μm. Here, $\mathbf{n}_{\mathbf{x}_i^G}$ is the outward normal vector to the membrane at point $\mathbf{x}_i^G$. Note that the penalty function is sensitive to the signs of the angles that must be consistently measured. For the 3D case, we proceed analogously, but the penalty function is given by $PF_{3\text{D}}(\mathbf{x}_i^G) = |\widehat{\mathbf{n}_q, \mathbf{n}_{\mathbf{x}_i^G}} - \omega_i| + |\widehat{\mathbf{n}_{\mathbf{s}_i^*}, \mathbf{n}_{\mathbf{x}_i^G}} - \beta\omega_i^*| + 1.5 d_{\mathbf{s}_i^*}(\mathbf{x}_i^G) + 100\,[\mathbf{n}_q, \mathbf{n}_{\mathbf{s}_i^*}, \mathbf{n}_{\mathbf{x}_i^G}]$ where $[\mathbf{n}_q, \mathbf{n}_{\mathbf{s}_i^*}, \mathbf{n}_{\mathbf{x}_i^G}]$ represents the volume of the parallelepiped defined by the vectors $\mathbf{n}_q$, $\mathbf{n}_{\mathbf{s}_i^*}$, and $\mathbf{n}_{\mathbf{x}_i^G}$ in μm^3.

A4: Parameter values used in the simulations

The values of the model parameters used in the 2D examples are listed in Table 1. The values used in the 3D examples are identical, except for those parameters listed in Table 2. Three parameters present significant differences, namely $\overline{\eta}_f$, $\overline{\eta}_m$, and R_a. The protrusive ($\overline{\eta}_f$) and contractile ($\overline{\eta}_m$) forces are adjusted to reproduce biological velocities, while the activator source radius (R_a) is modified to achieve realistic pseudopod size in the simulations. We believe that the mismatch between parameters in two and three dimensions may be attributed to membrane forces. Membrane forces depend on the membrane's curvature which varies substantially from

Table 1 Parameters used in the 2D examples

Symbol	Description	Value/References
Experimentally observed		
$D_m^{\max}$	Myosin diffusion scale	$4.16\ \mu m^2 s^{-1}$ [a]
μ	Dynamic viscosity coefficient	$1500\ pN\,s\,\mu m^{-1}$ [b]
λ	Bulk viscosity coefficient	$-500\ pN\,s\,\mu m^{-1}$ [b]
$\overline{\eta}_m$	Strength of contractile forces	$22\ pN\,\mu m$ [c]
γ	Surface tension coefficient	$78\ pN$ [d]
D_a	Diffusion coefficient of activator	$0.2\ \mu m^2 s^{-1}$ [a]
R_a	Radius of activator source	$1\ \mu m$ [e]
Computationally estimated		
Γ_ϕ	Phase-field Lagrange multiplier	$0.52\ \mu m\,s^{-1}$ [f]
ε	Phase-field interfacial length scale	$2\ \mu m$ [f]
φ	Scaling of membrane marker width	20
K_m	Decay rate of myosin diffusion	$1.55\ \mu m^2$ [f]
ε_f	Diffusive length scale of F-actin	$1\ \mu m$ [g]
ε_g	Diffusive length scale of G-actin	$3.16\ \mu m$ [g]
Γ_f	F-actin mobility	$0.52\ s^{-1}$ [g]
Γ_g	G-actin mobility	$0.52\ s^{-1}$ [g]
α_f	Range of protrusive forces	0.075 [g]
$\overline{\eta}_f$	Strength of protrusive forces	$12,000\ pN\,\mu m^3$ [g]
α_m	Range of contractile forces	0.41 [g]
ς	Substrate drag coefficient	$0.7\ pN\,s\,\mu m^{-3}$ [h]
η_{rep}	Strength of repulsive forces	$6000\ pN\,\mu m$ [g]
r_q	Decay rate of chemoattractant	$0.1\ s^{-1}$
b_q	Production rate of chemoattractant	$500\ s^{-1}$
k_q	Consumption rate of chemoattractant	$10\ s^{-1}$
r_a	Decay rate of activator	$0.32\ s^{-1}$ [g]
b_a	Production rate of activator	$7.8\ s^{-1}$ [g]

The parameters are classified according to the methodology used to measure their values
[a]Petrášek et al. (2008)
[b]Bausch et al. (1998)
[c]Rubinstein et al. (2009)
[d]Tinevez et al. (2009)
[e]Ura et al. (2012)
[f]Shao et al. (2012)
[g]Moure and Gomez (2016, 2017)
[h]Camley et al. (2013)
[i]Buenemann et al. (2010)

two to three dimensions (one principal curvature is zero in 2D). Table 2 also includes the parameters used only in the 3D examples. The parameters not listed here may be found in the main text.

A5: Description of cAMP waves

Here, we define the nondissipating waves used in Sect. 4.2 to replicate the experiments in Skoge et al. (2014). The experiments correspond to a wave traveling in the direction of a channel, which we assume to be aligned with the x axis. The chemoattractant wave has a wavelength $\lambda_q = 1300\ \mu m$, a maximum concentration $Q = 700$ nM, and moves with velocity $\{-\lambda_q/T_w, 0\}^T\ \mu m/s$, where T_w is the period of the wave. The concentration of a single wave can be defined as

$$q(x,t) = Q \exp\left[-0.5\left(\frac{x + \frac{\lambda_q}{T_w}t - \frac{\lambda_q}{2}}{\sigma_q}\right)^2\right], \tag{28}$$

with the constant $\sigma_q = 101.12\ \mu m$. If we consider a set of waves that are λ_q away from each other in the x-direction,

Table 2 Parameters used in the 3D examples

Symbol	Description	Value/References
K_m	Decay rate of myosin diffusion	1.55 μm^3 [f]
μ	Dynamic viscosity coefficient	1500 pN s μm^{-2} [b]
λ	Bulk viscosity coefficient	-500 pN s μm^{-2} [b]
$\overline{\eta}_f$	Strength of protrusive forces	11, 400 pN μm^3 [g]
$\overline{\eta}_m$	Strength of contractile forces	9.9 pN μm [c]
ς	Drag coefficient	0.7 pN s μm^{-4}
N_{adh}	Maximum number of adhesions	100 [i]
k_{grip_0}	Gripping coefficient	1.5 pN s^{-1} μm^{-1} [h]
r_{off_0}	Disassociation rate of adhesions	0.002 s^{-1} [i]
F_0	Characteristic adhesive strength	12 pN μm^{-3} [h]
γ	Surface tension coefficient	78 pN μm^{-1} [d]
η_{rep}	Strength of repulsive forces	6000 pN
R_a	Radius of activator source	2 μm [e]

We show the parameters that change with respect to Table 1 and the parameters used only in the 3D examples. The references are listed in Table 1

the concentration of each wave i is given by

$$q_i(x,t) = Q \exp\left[-0.5 \left(\frac{x + \frac{\lambda_q}{T_w} t - (2i-1)\frac{\lambda_q}{2}}{\sigma_q} \right)^2 \right], \tag{29}$$

where i is a positive integer that identifies each wave. The distribution q used in Sect. 4.2 can be computed as $q(x,t) = \sum_i q_i(x,t)$, where i accounts for the waves with non-zero concentration in the vicinity of the cell.

References

Allena R, Aubry D (2012) 'Run-and-tumble' or 'look-and-run'? A mechanical model to explore the behavior of a migrating amoeboid cell. J Theor Biol 306:15–31

Andrew N, Insall RH (2007) Chemotaxis in shallow gradients is mediated independently of ptdins 3-kinase by biased choices between random protrusions. Nat Cell Biol 9(2):193

Bausch AR, Ziemann F, Boulbitch AA, Jacobson K, Sackmann E (1998) Local measurements of viscoelastic parameters of adherent cell surfaces by magnetic bead microrheometry. Biophys J 75(4):2038–2049

Bell GI (1978) Models for the specific adhesion of cells to cells. Science 200:618–627

Biben T, Kassner K, Misbah C (2005) Phase-field approach to three-dimensional vesicle dynamics. Phys Rev E 72(041):921

Bosgraaf L, Van Haastert PJM (2009a) Navigation of chemotactic cells by parallel signaling to pseudopod persistence and orientation. PLoS ONE 4:e6842

Bosgraaf L, Van Haastert PJM et al (2009b) The ordered extension of pseudopodia by amoeboid cells in the absence of external cues. PLoS ONE 4:e5253

Buenemann M, Levine H, Rappel WJ, Sander LM (2010) The role of cell contraction and adhesion in dictyostelium motility. Biophys J 99(1):50–58

Camley BA, Zhao Y, Li B, Levine H, Rappel WJ (2013) Periodic migration in a physical model of cells on micropatterns. Phys Rev Lett 111(158):102

Casquero H, Bona-Casas C, Gomez H (2017) NURBS-based numerical proxies for red blood cells and circulating tumor cells in microscale blood flow. Comput Methods Appl Mech Eng 316:646–667

Chen BC, Legant WR, Wang K, Shao L, Milkie DE, Davidson MW, Janetopoulos C, Wu XS, Hammer JA III, Liu Z, English BP, Mimori-Kiyosue Y, Romero DP, Ritter AT, Lippincott-Schwartz J, Fritz-Laylin L, Dyche Mullins R, Mitchell DM, Bembenek JN, Reymann AC, Böhme R, Grill SW, Wang JT, Seydoux G, Serdar Tulu U, Kiehart DP, Betzig E (2014) Lattice light-sheet microscopy: imaging molecules to embryos at high spatiotemporal resolution. Science 346(1257):998

Choi CK, Vicente-Manzanares M, Zareno J, Whitmore LA, Mogilner A, Horwitz AR (2008) Actin and α-actinin orchestrate the assembly and maturation of nascent adhesions in a myosin II motor-independent manner. Nat Cell Biol 10:1039–1050

Chung J, Hulbert GM (1993) A time integration algorithm for structural dynamics with improved numerical dissipation: the generalized-α method. J Appl Mech 60:371–375

Dawes AT, Edelstein-Keshet L (2007) Phosphoinositides and Rho proteins spatially regulate actin polymerization to initiate and maintain directed movement in a one-dimensional model of a motile cell. Biophys J 92:744–768

del Álamo JC, Meili R, Alonso-Latorre B, Rodríguez-Rodríguez J, Aliseda A, Firtel RA, Lasheras JC (2007) Spatio-temporal analysis of eukaryotic cell motility by improved force cytometry. Proc Natl Acad Sci USA 104:13,343–13,348

Elliott CM, Stinner B, Venkataraman C (2012) Modelling cell motility and chemotaxis with evolving surface finite elements. J R Soc Interface 9:3027–3044

Friedl P, Wolf K (2003) Tumour-cell invasion and migration: diversity and escape mechanisms. Nat Rev Cancer 3:362–374

Friedl P, Wolf K (2009) Plasticity of cell migration: a multiscale tuning model. J Cell Biol 188:11–19

Fuller D, Chen W, Adler M, Groisman A, Levine H, Rappel WJ (2010) External and internal constraints on eukaryotic chemotaxis. Proc Natl Acad Sci USA 107:9656–9659

Gamba A, de Candia A, Di Talia S, Coniglio A, Bussolino F, Serini G (2005) Diffusion-limited phase separation in eukaryotic chemotaxis. Proc Natl Acad Sci USA 102:16,927–16,932

Geiger B, Spatz JP, Bershadsky AD (2009) Environmental sensing through focal adhesions. Nat Rev Mol Cell Biol 10:21–33

Goldstein RE (1996) Traveling-wave chemotaxis. Phys Rev Lett 77:775

Gomez H, van der Zee K (2017) Computational phase-field modeling. Encyclopedia of Computational Mechanics, accepted for publication

Hecht I, Skoge ML, Charest PG, Ben-Jacob E, Firtel RA, Loomis WF, Levine H, Rappel WJ (2011) Activated membrane patches guide chemotactic cell motility. PLoS Comput Biol 7(e1002):044

Hughes TJR, Cottrell JA, Bazilevs Y (2005) Isogeometric analysis: CAD, finite elements, NURBS, exact geometry and mesh refinement. Comput Methods Appl Mech Eng 194:4135–4195

Insall RH (2010) Understanding eukaryotic chemotaxis: a pseudopod-centred view. Nat Rev Mol Cell Biol 11:453–458

Janetopoulos C, Ma L, Devreotes PN, Iglesias PA (2004) Chemoattractant-induced phosphatidylinositol 3,4,5-trisphosphate accumulation is spatially amplified and adapts, independent of the actin cytoskeleton. Proc Natl Acad Sci USA 101:8951–8956

Jansen K, Whiting C, Hulbert G (2000) Generalized-α method for integrating the filtered Navier–Stokes equations with a stabilized finite element method. Comput Methods Appl Mech Eng 190:305–319

Jurado C, Hasserick JR, Lee J (2005) Slipping or gripping? fluorescent speckle microscopy in fish keratocytes reveals two different mechanisms for generating a retrograde flow of actin. Mol Biol Cell 16:507–518

Lämmermann T, Sixt M (2009) Mechanical modes of 'amoeboid' cell migration. Curr Opin Cell Biol 21:636–644

Lämmermann T, Bader BL, Monkley SJ, Worbs T, Wedlich-Söldner R, Hirsch K, Keller M, Förster R, Critchley DR, Fässler R et al (2008) Rapid leukocyte migration by integrin-independent flowing and squeezing. Nature 453(7191):51

Levchenko A, Iglesias PA (2002) Models of eukaryotic gradient sensing: application to chemotaxis of amoebae and neutrophils. Biophys J 82:50–63

Levine H, Kessler DA, Rappel WJ (2006) Directional sensing in eukaryotic chemotaxis: a balanced inactivation model. Proc Natl Acad Sci USA 103:9761–9766

Li X, Lowengrub J, Rätz A, Voigt A (2009) Solving PDEs in complex geometries: a diffuse domain approach. Commun Math Sci 7:81–107

Liu WK, Liu Y, Farrell D, Zhang L, Wang XS, Fukui Y, Patankar N, Zhang Y, Bajaj C, Lee J, Hong J, Chen X, Hsu H (2006) Immersed finite element method and its applications to biological systems. Comput Methods Appl Mech Eng 195:1722–1749

MacDonald G, Mackenzie JA, Nolan M, Insall RH (2016) A computational method for the coupled solution of reaction-difusion equations on evolving domains and manifolds: application to a model of cell migration and chemotaxis. J Comput Phys 309:207–226

Marée AFM, Grieneisen VA, Edelstein-Keshet L (2012) How cells integrate complex stimuli: the effect of feedback from phosphoinositides and cell shape on cell polarization and motility. PLoS Comput Biol 8(e1002):402

Marth W, Voigt A (2014) Signaling networks and cell motility: a computational approach using a phase field description. J Math Biol 69:91–112

Meinhardt H (1999) Orientation of chemotactic cells and growth cones: models and mechanisms. J Cell Sci 112:2867–2874

Mori Y, Jilkine A, Edelstein-Keshet L (2008) Wave-pinning and cell polarity from a bistable reaction-diffusion system. Biophys J 94:3684–3697

Moure A, Gomez H (2016) Computational model for amoeboid motion: coupling membrane and cytosol dynamics. Phys Rev E 94(042):423

Moure A, Gomez H (2017) Phase-field model of cellular migration: three-dimensional simulations in fibrous networks. Comput Methods Appl Mech Eng 320:162–197

Neilson MP, Veltman DM, van Haastert PJM, Webb SD, Mackenzie JA, Insall RH (2011) Chemotaxis: a feedback-based computational model robustly predicts multiple aspects of real cell behaviour. PLoS Biol 9(e1000):618

Novak IL, Slepchenko BM, Mogilner A (2008) Quatitative analysis of G-actin transport in motile cells. Biophys J 95:1627–1638

Petrášek Z, Hoege C, Mashaghi A, Ohrt T, Hyman AA, Schwille P (2008) Characterization of protein dynamics in asymmetric cell division by scanning fluorescence correlation spectroscopy. Biophysical J 95(11):5476–5486

Ribeiro FO, Gómez-Benito MJ, Folgado J, Fernandes PR, García-Aznar JM (2017) Computational model of mesenchymal migration in 3D under chemotaxis. Comput Methods Biomech Biomed Eng 20:59–74

Rubinstein B, Fournier MF, Jacobson K, Verkhovsky AB, Mogilner A (2009) Actin-myosin viscoelastic flow in keratocyte lamellipod. Biophys J 97:1853–1863

Shao D, Levine H, Rappel WJ (2012) Coupling actin flow, adhesion, and morphology in a computational cell motility model. Proc Natl Acad Sci USA 109:6851–6856

Shi C, Huang CH, Devreotes PN, Iglesias PA (2013) Interaction of motility, directional sensing, and polarity modules recreates the behaviors of chemotaxing cells. PLoS Comput Biol 9(e1003):122

Skoge M, Yue H, Erickstad M, Bae A, Levine H, Groisman A (2014) Cellular memory in eukaryotic chemotaxis. Proc Natl Acad Sci USA 111:14,448–14,453

Song L, Nadkarni SM, Bödeker HU, Beta C, Bae A, Franck C, Rapper WJ, Loomis WF, Bodenschatz E (2006) Dictyostelium discoideum chemotaxis: threshold for directed motion. Eur J Cell Biol 85:981–989

Strychalski W, Copos CA, Lewis OL, Guy RD (2015) A poroelastic immersed boundary method with applications to cell biology. J Comput Phys 282:77–97

Subramanian KK, Narang A (2004) A mechanistic model for eukaryotic gradient sensing: spontaneous and induced phosphoinositide polarization. J Theor Biol 231:49–67

Sunyer R, Conte V, Escribano J, Elosegui-Artola A, Labernadie A, Valon L, Navajas D, García-Aznar JM, Muñoz JJ, Roca-Cusachs P et al (2016) Collective cell durotaxis emerges from long-range intercellular force transmission. Science 353(6304):1157–1161. https://doi.org/10.1126/science.aaf7119

Swaney KF, Huang CH, Devreotes PN (2010) Eukaryotic chemotaxis: a network of signaling pathways controls motility, directional sensing, and polarity. Annu Rev Biophys 39:265–289

Swanson JA, Taylor DL (1982) Local and spatially coordinated movements in dictyostelium discoideum amoebae during chemotaxis. Cell 28(2):225–232

Teigen KE, Li X, Lowengrub J, Wang F, Voigt A (2009) A diffuse-interface approach for modeling transport, diffusion and adsorption/desorption of material quantities on a deformable interface. Commun Math Sci 4:1009–1037

Tinevez JY, Schulze U, Salbreux G, Roensch J, Joanny JF, Paluch E (2009) Role of cortical tension in bleb growth. Proc Natl Acad Sci 106(44):18,581–18,586

Tjhung E, Tiribocchi A, Marenduzzo D (2015) A minimal physical model captures the shapes of crawling cells. Nat Commun 6:5420

Tweedy L, Meier B, Stephan J, Heinrich D, Endres RG (2013) Distinct cell shapes determine accurate chemotaxis. Sci Rep 3:2606

Ura S, Pollitt AY, Veltman DM, Morrice NA, Machesky LM, Insall RH (2012) Pseudopod growth and evolution during cell movement

is controlled through SCAR/WAVE dephosphorylation. Curr Biol 22(7):553–561
Van Haastert PJM (2010) A stochastic model for chemotaxis based on the ordered extension of pseudopods. Biophys J 99:3345–3354
Van Haastert PJM, Devreotes PN (2004) Chemotaxis: signalling the way forward. Nat Rev Mol Cell Biol 5:626–634
Vermolen FJ, Gefen A (2013) A phenomenological model for chemico-mechanically induced cell shape changes during migration and cell–cell contacts. Biomech Model Mechanobiol 12:301–323
Wessels D, Brincks R, Kuhl S, Stepanovic V, Daniels KJ, Weeks G, Lim CJ, Spiegelman G, Fuller D, Iranfar N, Loomis WF, Soll DR (2004) RasC plays a role in transduction of temporal gradient information in the cyclic-AMP wave of Dictyostelium discoideum. Eukaryot Cell 3:646–662
Ziebert F, Aranson IS (2016) Computational approaches to substrate-based cell motility. npj Comput Mater 2:16,019